

AEDC-TR-68-110

ARCHIVE COPY
DO NOT LOAN

cy 1

DOC_NOM SER CN

UNC22508-PDC A 1



MEASUREMENTS OF CONDENSATION
AND EVAPORATION OF CARBON DIOXIDE,
NITROGEN, AND ARGON AT CRYOGENIC
TEMPERATURES USING A MOLECULAR BEAM



J. H. Heald, Jr. and R. F. Brown

ARO, Inc.

September 1968

PROPERTY OF U. S.
ASDC LIBRARY
F40600-69-C-0001
AIR FORCE

This document has been approved for public release
and sale; its distribution is unlimited.

AEROSPACE ENVIRONMENTAL FACILITY
ARNOLD ENGINEERING DEVELOPMENT CENTER
AIR FORCE SYSTEMS COMMAND
ARNOLD AIR FORCE STATION, TENNESSEE

PROPERTY OF U. S. AIR FORCE
ASDC LIBRARY
F40600-69-C-0001

AEDC TECHNICAL LIBRARY



NOTICES

When U. S. Government drawings specifications, or other data are used for any purpose other than a definitely related Government procurement operation, the Government thereby incurs no responsibility nor any obligation whatsoever, and the fact that the Government may have formulated, furnished, or in any way supplied the said drawings, specifications, or other data, is not to be regarded by implication or otherwise, or in any manner licensing the holder or any other person or corporation, or conveying any rights or permission to manufacture, use, or sell any patented invention that may in any way be related thereto.

Qualified users may obtain copies of this report from the Defense Documentation Center.

References to named commercial products in this report are not to be considered in any sense as an endorsement of the product by the United States Air Force or the Government.

MEASUREMENTS OF CONDENSATION
AND EVAPORATION OF CARBON DIOXIDE,
NITROGEN, AND ARGON AT CRYOGENIC
TEMPERATURES USING A MOLECULAR BEAM

J. H. Heald, Jr. and R. F. Brown
ARO, Inc.

This document has been approved for public release
and sale; its distribution is unlimited.

FOREWORD

The research presented in this report was sponsored by the Arnold Engineering Development Center (AEDC), Air Force Systems Command (AFSC), Arnold Air Force Station, Tennessee, under Program Element 6144501F, Project 8951, Task 895104.

The results presented were obtained by ARO, Inc. (a subsidiary of Sverdrup & Parcel and Associates, Inc.), contract operator of AEDC, AFSC, under Contract F40600-69-C-0001. The research was conducted from October, 1966, to July, 1967, under ARO Project No. SW5801. The manuscript was submitted for publication on April 23, 1968.

Grateful acknowledgement is extended to Prof. R. E. Stickney of the Massachusetts Institute of Technology for his valuable consultations concerning the mechanism of heterogeneous condensation and the interpretation of experimental data.

This technical report has been reviewed and is approved.

Terry L. Hershey
Captain, USAF
Research Division
Directorate of Plans
and Technology

Edward R. Feicht
Colonel, USAF
Director of Plans
and Technology

ABSTRACT

A high intensity, aerodynamic molecular beam generator combined with a sensitive modulated beam detector has been used in the study of the condensation and evaporation processes of carbon dioxide, nitrogen, and argon (CO_2 , N_2 , and Ar) on cryogenically cooled surfaces. Molecular beams of intensities between 10^{13} and 10^{16} molecules/sec-cm² which correspond to gas pressures between 10^{-8} and 10^{-5} torr have been impinged on a polished copper target at surface temperatures between 20 and 300°K. The results of these experiments have shown that: (1) Room temperature molecular beams of CO_2 , N_2 , and Ar scattered from a copper surface at temperatures below 300°K follow a cosine law scattering pattern. The scattering pattern remains unchanged after the initiation of condensation and also during the evaporation process. The scattering pattern was insensitive to angle of incidence for angles between 0 and 80 deg relative to the surface normal. (2) The initiation of condensation of CO_2 , N_2 , and Ar gases on cryogenically cooled surfaces follows a definite gas pressure and surface temperature relation which is predicted by the theoretical relations derived by Frenkel. (3) The measured CO_2 evaporation rate between 75 and 95°K is in agreement with the extrapolation from published values at higher temperatures. (4) After initiation of condensation, the value of the capture coefficient is observed to approach a unity value. The high detector sensitivity allows measurements of capture coefficient up to 0.995.

CONTENTS

	<u>Page</u>
ABSTRACT	iii
NOMENCLATURE	vii
I. INTRODUCTION	1
II. APPARATUS	
2.1 Chamber and Beam Generation System	2
2.2 Target	2
2.3 Detection System.	3
III. PROCEDURE	
3.1 Spatial Distribution Measurement Technique	3
3.2 Condensation and Evaporation Measurement Technique.	4
IV. EXPERIMENTAL RESULTS AND DISCUSSION	
4.1 Beam Scattering and Evaporation Patterns	5
4.2 Condensation and Evaporation Experiments	7
4.3 Condensation Rate Experiments	18
V. CONCLUSIONS AND SUGGESTIONS.	24
REFERENCES.	26

TABLES

I. Comparison of Experimental and Published Values	13
II. Comparison of Experimental and Calculated Results	15

APPENDICES

I. ILLUSTRATIONS

Figure

1. Schematic of the AEDC Aerodynamic Molecular Beam Chamber	33
2. Target and Mass Spectrometer Arrangement	34
3. Ion Gage Used to Measure Incident Beam Intensity.	35
4. Schematic of Mass Spectrometric Modulated Beam Detector	36
5. Typical Condensation and Evaporation Experiment.	37

<u>Figure</u>	<u>Page</u>
6. Scattering Patterns at Near-Normal Incidence and Evaporation Flux Pattern	38
7. Scattering Patterns at 80-deg Incidence	39
8. Reflected Beam Signal versus Time after Initiation of Condensation	40
9. Reflected Beam Signal versus Surface Temperature after Initiation of Condensation for CO ₂	41
10. Characteristic Curves of CO ₂ Condensation and Evaporation.	42
11. Critical Supersaturation Ratios of CO ₂	43
12. Characteristic Curves of N ₂ and Ar Condensation	44
13. Critical Supersaturation Ratios of N ₂ and Ar	45
14. Critical Intensity of CO ₂ for Condensation	46
15. Critical Intensity of N ₂ and Ar for Condensation.	47
16. Data Correlation of CO ₂ to Theoretical Rate Equation	48
17. Data Correlation of CO ₂ to Modified Theoretical Equation	49
18. Beam Capture Coefficient of CO ₂ as a Function of Time after Initiation of Condensation	50
19. Beam Capture Coefficient of CO ₂ as a Function of Surface Temperature	51
20. Calculated Trapezoidal Beam Profile	52
21. Measured Incident Beam Profile	53
22. Calculated Reflected Gas Flux Dependence on Surface Temperature	54
23. Condensation Rate for High Intensity CO ₂ Beam.	55
24. Condensation Rate for Low Intensity CO ₂ Beam	56
25. Effect of Two Collimators on CO ₂ Beam Capture Coefficient	57
26. Effects of Two Collimators and Beam Intensity on Time-Dependent Signals for CO ₂	58

<u>Figure</u>	<u>Page</u>
27. Effects of Surface Temperature on Time-Dependent Signals for CO ₂	59
28. Beam Condensation of N ₂ and Ar	60
29. General Condensation and Evaporation Regions for CO ₂ between 72 and 90°K	61
II. CALCULATION OF MOLECULAR BEAM PRESSURE FROM BEAM INTENSITY.	62
III. CALCULATION OF DETECTOR CHOPPER WHEEL EFFECTS ON SCATTERED BEAM SPATIAL DISTRIBUTION PATTERNS	64
IV. CALCULATION OF BEAM INTENSITY PROFILE EFFECTS ON REFLECTED GAS FLUX.	66

NOMENCLATURE

a_0	Lattice parameter of the nucleus
ΔA	Increment of surface area being struck by beam intensity
ΔI_i	
C_b	Fraction of total incident beam flux which condenses on the target
C_i	Fraction of incident beam flux at one intensity which condenses on the target
F	Free energy
F_l	Free energy of liquid or condensate phase
F_v	Free energy of vapor phase
ΔF^*	Standard free energy of formation of the critical nuclei
ΔF_{ad}	Standard free energy of adsorption
ΔF_d	Free energy of activation for surface diffusion
$f(\theta)$	Function of the contact angle between the nucleus and substrate
H_0	Heat of adsorption

H_v	Heat of vaporization of paired molecules
ΔH_v	Heat of evaporation
I	Gas intensity, molecules/sec-cm ²
K	Detector calibration constant
k	Boltzmann constant
M	Molecular weight
m	Mass
\dot{N}_d	Gas flux entering detector, molecules/sec
\dot{N}_i	Incident gas flux, molecules/sec
\dot{N}_r	Reflected gas flux, molecules/sec
\dot{N}_t	Total gas flux leaving the surface, molecules/sec
\dot{N}_v	Evaporation flux leaving the surface, molecules/sec
$\dot{\Delta N}_c$	Portion of the total incident beam flux which is being condensed, molecules/sec
P	Gas pressure
P_c	Critical gas pressure for the initiation of condensation
P_e	Equilibrium vapor pressure
P_i	Incident beam pressure
P_r	Reflected beam pressure
R	Gas constant
S	Entropy
S_R	Detector signal produced by reflected beam flux
T	Temperature
T_c	Critical surface temperature for the initiation of condensation
T_e	Surface temperature for equilibrium between evaporation and condensation flux rates
T_s	Surface temperature
U	Internal energy
V	Volume of condensate phase
v	Volume of vapor phase and specific volume of vapor phase

γ	Free energy per unit area of the interface between nucleus and vapor
θ	Contact angle between surface of condensation nucleus and plane of substrate
θ_d	Angle of reflection measured from the surface normal
ν	Vibration frequency of the surface atoms
ρ	Density
σ_0	Cross section of the atom
τ	Adsorption time of gas molecule sticking a surface
τ_0	Period of oscillation of an atom adsorbed on the substrate surface
$d\omega$	Element of solid angle subtended by the detector

SECTION I INTRODUCTION

During the past 10 yr, cryopumping has been widely employed in the production of the vacuum environment, and investigators (Refs. 1 through 9) have measured the condensation rates for various gases on a cryosurface. They reported data in terms of a capture coefficient, and widely varying values have been observed (Refs. 1, 5, 7, 8, and 9).

At first, when conflicting values were reported, it was generally assumed that experimental error was responsible for the disagreement. However, as bare surface effects and variation of the condensation rate with gas purity, gas temperature, and cryosurface temperature were reported later (Refs. 1, 4, 10, and 11), it became evident that many of the published variations in values of the capture coefficient for a particular gas species were probably the result of unnoticed variations in the experimental conditions (Ref. 8).

Thus far, most of the capture coefficients have been obtained by making measurements of the total pumping speed of the cryosurface (Ref. 1) and then ratioing the measured pumping speed to the theoretical speed predicted by kinetic theory. These experiments have been generally limited to random flow to the cryosurface and a narrow range of gas temperatures (usually 200 to 400°K). The success of the experiments has depended on an absolute calibration of the metering device or a pressure gage. Measurements of this type have provided useful data, but they have not provided the accurate data needed in developing a good theoretical model of the condensation phenomenon.

In order to study the condensation process of gases under carefully controlled conditions, a high intensity molecular beam chamber has been constructed at AEDC (Ref. 12). The molecular beam technique has made possible the independent variation of surface and gas properties over a wide range of temperature, pressure, gas species, geometric orientation between gas and surface, and surface configuration. Hence, any dependence of condensation on any one variable can be independently studied.

This chamber is being used to provide accurate condensation rate data for several gases as the gas temperature is varied from 300 to 1500°K, the angle of incidence is varied from 0 to 90 deg, and the target temperature is varied from 300 to 10°K. Several other parameters such as background gas species, deposit thickness, beam intensity, and velocity distributions of the beam will also be systematically varied to determine if they affect the capture coefficient.

The data presented and discussed in this report include: (1) the surface temperature at which condensation begins for beams of carbon dioxide (CO_2), nitrogen (N_2), and argon (Ar), (2) the effect of the beam intensity on the temperature at which condensation begins, (3) the evaporation rates of beam deposits in a vacuum, (4) the spatial distribution of evaporation flux and reflected beams, (5) the critical supersaturation ratio required to initiate the condensation process, (6) the rate of condensation, and (7) comparison of the observed results with existing condensation theories and other experimental results.

SECTION II APPARATUS

2.1 CHAMBER AND BEAM GENERATION SYSTEM

The AEDC Aerodynamic Molecular Beam Chamber (Fig. 1, Appendix I) is a stainless steel cylinder, 3 ft in diameter by 6.5 ft long, which is divided into three sections by two removable bulkheads. Vacuum conditions are produced and maintained in the cell by oil diffusion pumps, 20°K gaseous-helium (GHe)-cooled cryoliners, and 77°K liquid-nitrogen (LN_2)-cooled cryoliners. The total pumping speed for air is in excess of 500,000 liters/sec.

This system is capable of producing a 4-mm-diam beam entering the test section with a variable beam flux from 1.0×10^{13} to 2.0×10^{16} molecules/sec while maintaining a background pressure of 10^{-8} torr in the test section.

The beam-generating components consist of a 0.5-mm-diam nozzle source, a 4-mm-diam conical skimmer located 42.7 mm downstream from the nozzle, and a 4-mm-diam collimator positioned 473 mm downstream from the skimmer tip. A complete description of the beam system and its performance is given in Ref. 12.

2.2 TARGET

The target (Fig. 2) was fabricated from electrolytic copper, and the front was hand polished to an 8-microinch (μ in.) RMS finish. The target temperature was controlled by a continuous circulation of GHe from a variable temperature cryostat. Two chromel-constantan thermocouples and a germanium resistance thermometer imbedded in the target were used to measure the target temperature.

2.3 DETECTION SYSTEM

The molecular beam detection systems consist of an ionization gage for measuring the total incident beam flux (Fig. 3), and a modulated beam detector for measuring the reflected beam signals. The ionization gage was calibrated for absolute measurements of incident beam flux using a beam of known molecular flux as described in Ref. 12.

The modulated beam detection system employed consists of (1) a mechanical beam chopper, (2) a quadrupole mass spectrometer, and (3) a lockin amplifier (Fig. 4). This detector system has the capability of recovering the signal from beam intensities that are three orders of magnitude less than the background gas intensity. This detector responds only to total molecular flow rate and is insensitive to changes in molecular velocity. A complete description of the detector and its performance is given in Ref. 13.

SECTION III PROCEDURE

During a typical experiment, the chamber is pumped down to a pressure of 10^{-8} torr, and the beam is turned on. Then the source pressure is adjusted to give the desired beam intensity as measured by the calibrated ionization gage detector (Fig. 3). Typical chamber pressures during a test with the beam on and a source pressure of 200 torr are 2×10^{-8} torr, 1×10^{-7} torr, and 2×10^{-5} torr for the test, collimation, and nozzle discharge sections of the chamber, respectively.

3.1 SPATIAL DISTRIBUTION MEASUREMENT TECHNIQUE

In the first set of experiments the modulated beam detector was rotated about the target surface to measure the reflected or evaporated gas flux spatial distribution. The detector was mounted to rotate in the plane formed by the incident beam and the target surface normal with the center of rotation at the center of the incident beam impingement point on the target surface. The target surface was also rotated to vary the angle of incidence between 0 and 80 deg as measured from the surface normal. For these experiments the target was set to form a given angle of incidence, a beam was directed on the target, and the reflected gas flux spatial distribution was measured by rotating the detector. The surface temperature was also varied from room temperature down to temperatures sufficiently low to cause condensation of the incident beam, and

reflected beam spatial distributions were measured as a function of surface temperature. In order to measure the spatial distribution pattern of an evaporating gas flux, the surface was cooled until condensation of the incident beam began. The incident beam was used to deposit gas on the surface for several minutes and then shut off. Measurements were then made of the spatial distribution of the gas flux evaporating from this deposit spot.

3.2 CONDENSATION AND EVAPORATION MEASUREMENT TECHNIQUE

In the series of experiments to measure the conditions under which beam condensation occurs, the target was set at a fixed angle of beam incidence, and the detector was set at a fixed angle of reflection. A room temperature molecular beam of constant intensity was then directed onto the target surface, which was also at room temperature. In this case no beam condensation would occur, and the total incident beam was reflected. The incident beam was cycled on and off by moving the metal disk into and out of the path of the beam.

With this experimental setup, the target surface was then slowly cooled by the circulation of GHe from an external refrigerator through the interior of the target surface. The general nature of the resulting experimental data is depicted in Fig. 5. As the surface is cooled from room temperature (point 1), the reflected beam signal remains constant until the temperature at which condensation begins is reached (point 2). At this surface temperature, the reflected beam signal decreases, which indicates that deposition of the incident beam has begun.

If the surface temperature represented by point 2 is held constant, the reflected gas intensity decreases with time toward point 3, which indicates that an increasing amount of the incident beam is being deposited. Any further cooling of the surface will also decrease the reflected signal, as indicated by the line between points 3 and 4. At some lower surface temperature, the reflected beam signal becomes immeasurably low, as determined by the detector sensitivity. For these experiments the modulated beam detector could measure reflected beam signals as low as 5×10^{-3} times the magnitude of the reflected beam signal before condensation began (point 2).

After condensation of the incident beam has begun, the surface can be warmed, and the reflected or evaporated gas intensity can be measured as represented by the curve between points 3 and 5. If the surface is warmed after condensation has occurred, the gas intensity entering the detector increases but remains less than the initial (point 2) value

up to some temperature (point 5) which is greater than the temperature at which condensation began (point 2). A flux equilibrium temperature is defined at point 5 where the incident beam flux equals the total flux leaving the surface.

The evaporation flux leaving the deposit spot is another measurement made after the beam had deposited on the target. If the incident beam is turned off, the remaining gas flux entering the detector is produced by evaporation from the condensed beam gas. The surface temperature can be varied, and a plot of evaporation flux versus surface temperature can be made (curve 6).

SECTION IV EXPERIMENTAL RESULTS AND DISCUSSION

4.1 BEAM SCATTERING AND EVAPORATION PATTERNS

Since the modulated beam detector (as depicted in Fig. 2) can only measure a small geometric portion of any gas flux leaving the target surface, it is essential to measure any desired gas property in terms of angle of reflection to detect any possible variations of gas properties with angle of reflection. Also, with the target movable, any possible dependence of reflected gas properties on angle of incidence can be measured.

In Fig. 6 typical scattering patterns are shown for a beam of CO_2 gas molecules striking at near-normal incidence. The molecular beam strikes the target surface at an angle of incidence of 10 deg measured relative to the surface normal. The data points indicated by the circles represent the relative gas intensity at various angles of reflection for a CO_2 beam from a 300°K target surface. The target was a polished copper surface which had undergone no special cleaning process before the beam scattering experiments. The surface was then microscopically rough and covered with any test chamber gases which had been absorbed during the pumpdown process to the vacuum pressure of approximately 1×10^{-8} torr. As can be seen, the scattering pattern under these conditions is near circular, indicating that the scattering process is representative of the cosine law for random reflection.

For the data taken with the target at 77°K, about 50 percent of the incident beam flux was being condensed. The data points represent the relative gas intensity at various angles of reflection for the portion of the incident beam which is not condensed but scattered by the surface. Once again, the data follow the cosine law scattering pattern.

At a surface temperature of 77°K, the CO₂ beam was allowed to condense on the target for about 30 min; then the beam was shut off, and the surface was slowly warmed until the CO₂ gas flux evaporating from the deposit spot was sufficiently large to produce measurable signals at the detector. The target was then held at a constant temperature of 85°K, and the spatial distribution of the evaporating gas flux was measured. As indicated by the solid dot data points, the distribution pattern appears to follow the cosine law for evaporation from a CO₂ deposit spot.

Several similar measurements were then made as the CO₂ beam angle of incidence was increased as measured from the surface normal. Since all angles of incidence appeared to give the same results, only those data at the highest angle of incidence will be discussed. In Fig. 7 the results of beam scattering measurements are shown which were made at a CO₂ beam angle of incidence of 80 deg and surface temperatures of 300 and 77°K. In both cases, for the noncondensing target as well as the condensing target surface, the reflected gas spatial distribution closely follows the calculated cosine law curve.

For high angles of incidence, the incident beam is spread out over a wide portion of the target surface. Since the chopper wheel is mounted between the target and the detector and has only a 0.5-in. opening, the chopper blocks part of the reflected gas from the surface when the beam spot on the target exceeds a certain diameter. The fraction of reflected beam blockage can be calculated for various angles of incidence as shown in Appendix III, and this correction can be applied to the theoretical cosine law values. The solid line in Fig. 7 represents a cosine law scattering corrected for the chopper wheel blockage.

Since molecular beams have been used for many years to measure the scattering patterns for various gas-surface interactions, it is interesting to compare the results of these measurements to those of other investigators. As discussed in the survey paper by Stickney (Ref. 14), the cosine law scattering pattern for neutral gas-solid surface interactions is generally observed unless (1) the target surface undergoes some special preparation process before interaction with the beam, such as extensive heating to remove adsorbed gases, or a cleaved crystal similarly cleaned is used as a target surface, or (2) a high energy beam is used with molecular velocities about ten times as great as velocities produced by expansion from a room temperature beam source. Under such conditions noncosine law scattering patterns have been frequently observed, generally in the form of a lobular-shaped pattern. Since neither of the above-mentioned conditions was met, the cosine law scattering was an expected result. However, for

the case of a beam scattering from a freshly deposited CO₂ spot, it was unknown whether the CO₂ condensate might act as a very clean smooth surface, especially if a crystal deposit were to occur. It was interesting then to observe that for this condition, cosine law scattering also occurred. The observed cosine law distribution for the gas flux evaporating from a condensate spot into a vacuum was also anticipated since some very early work by Knudsen and Wood (Refs. 15 and 16) using metal vapors produced the same result. However, this may be the first time such evaporating distribution patterns have been measured for atmospheric gases at low temperatures and pressures using a scanning molecular beam detector.

4.2 CONDENSATION AND EVAPORATION EXPERIMENTS

Several experiments were conducted to determine the conditions under which condensation of CO₂, N₂, and Ar would occur at cryogenic temperatures and high vacuum pressures. In addition, the evaporation flux from a CO₂ deposit was measured as a function of surface temperature. For the experiments reported herein, the onset of condensation has been measured as a function of beam intensity, beam species, angle of incidence, and surface temperature of a polished copper target. All experiments were conducted with a room temperature beam source. As in the previously discussed scattering experiments, no special surface preparation had been undertaken in terms of surface cleaning by heating or surface finishing beyond normal machine shop polishing to a mirror finish.

4.2.1 Beam Pressure Calculations

It is often useful to convert the beam intensity into a beam pressure acting on the target surface, since most condensation experimentation and theoretical treatment have been undertaken with gas pressure as a parameter. In this report the term "flux" will always refer to molecular flow rate (molecules/sec), whereas the term "intensity" will refer to flux per unit area (molecules/sec-cm²). For a gas at equilibrium within a closed container, the kinetic theory relation between pressure and intensity is:

$$P = I \sqrt{2\pi mkT} \quad (1)$$

where T is the gas and surface temperature. However, this relation will generally not be a precise calculation of pressure for an aerodynamically generated molecular beam because (1) the gas does not approach the target randomly but is highly directed, (2) the velocities

of the beam molecules are slightly higher than the equilibrium condition determined by the source temperature, and (3) the beam temperature will not always be equal to the surface temperature. A more precise relationship for beam pressure calculated from beam intensity is derived in Appendix II by considering the beam pressure as the sum of the incident and reflected beam pressures:

$$P = P_i + P_r \quad (2)$$

Using the velocity distribution for incident and reflected beam molecules, beam pressure has been calculated as a function of beam intensity and temperature as a function of the beam and target surface. Using the Maxwell-Boltzman equilibrium distribution in Eq. (2) gives the relation of Eq. (1), but considering an aerodynamic molecular beam for P_i gives a pressure about twice the magnitude of that calculated from Eq. (1) for a room temperature beam and target surface. Therefore, Eq. (1) relates only a correspondence in intensity between beam conditions and equilibrium conditions. If the velocity dependence of pressure is important to any observed phenomenon, Eq. (1) is not a precise method of calculating beam pressure. The dependence of condensation phenomena on the incident beam velocity will be the subject of future experimentation. For the purposes of this report, Eq. (1) has been used to convert to an equivalent equilibrium pressure which would produce the same gas intensity on a surface as that produced by the incident molecular beam.

4.2.2 Surface Temperatures and Beam Intensities to Initiate Condensation

With the target surface near room temperature, a constant intensity beam of CO_2 molecules generated from a room temperature source was allowed to strike the target surface. Under these conditions no condensation of the incident beam would occur, and the reflected gas flux (N_r) equals the incident beam flux (N_i). Since it was determined by the previously described scattering experiments that the spatial distribution of the reflected beam gas followed the cosine law for all conditions used in these experiments, the reflected gas flux entering the detector is given by:

$$\dot{N}_d = \frac{N_r}{\pi} \cos \theta_d d\omega \quad (3)$$

Therefore, as the surface is cooled, the reflected gas flux entering the detector will be proportional to the total flux leaving the surface as long as the detector remains in one fixed position relative to the surface.

With the constant intensity beam striking the target surface, the surface was slowly cooled, as described in Section III. The reflected

gas signal remains constant, indicating that the total incident beam flux is still being reflected. When the surface temperature at which condensation begins is reached, the detector signal decreases sharply, indicating some of the incident beam flux is being condensed on the surface. If the surface temperature is held constant at this point, the reflected gas signal decreases with time, as shown in Fig. 8, and indicates that the fraction of the incident beam being condensed is increasing with time*. If the surface temperature is further decreased, the reflected gas signal will also decrease until the signal is immeasurably low (Fig. 9).

The first parameter to be varied was the beam intensity. It was observed that as the beam intensity was increased, the temperature at which condensation begins also increased (Fig. 9). Several beam intensities were used which covered a range of over two orders of magnitude, as shown in Fig. 10, curve 1. As shown, the beam intensity required to initiate condensation on the bare surface varies in an exponential manner with the surface temperature.

As discussed in the previous section, changes in beam intensity correspond to changes in gas pressure on the surface. An experimental relation between temperature and pressure of a vapor in equilibrium with its condensate is generally expected as related by the classical Clausius-Clapeyron relation:

$$\frac{d(\ln P)}{dT} = \frac{\Delta H_v}{RT^2} \quad (4)$$

For this reason, published vapor pressure values for CO₂ (Ref. 17) have been converted to equivalent beam intensities using Eq. (1) and extrapolated into the range of intensities used. The resulting vapor intensity curve is shown as the dashed line in Fig. 10, curve 2. As shown, the vapor intensity curve nearly parallels the experimental curve for the intensity required to initiate condensation. A surface temperature about 7°K below the vapor pressure curve temperature is then required to initiate condensation of a CO₂ beam on a polished copper surface.

4.2.3 Evaporation Rate Measurements

4.2.3.1 Evaporation Rate into a Vacuum

Since the evaporation flux calculations were based on extrapolated vapor pressure data, it was important to experimentally determine the

*The plotted data have been normalized to the detector signal before the initiation of condensation.

magnitude of CO_2 evaporation flux into a vacuum over the temperature range of interest. After a heavy deposit of CO_2 had been formed on the target surface by an incident beam, the beam was shut off by dropping the metal disk into the path of the incident beam. Under these conditions, any measurable signal at the detector output would be caused by gas evaporating from the target surface into the surrounding vacuum. The evaporation flux signals were measured as a function of surface temperature and converted into gas intensity using a previously determined calibration constant. A beam of known intensity was generated as described in Ref. 12, and the reflected signal at a given detector location was measured. The calibration constant was taken as the constant of proportionality between the incident beam flux and the detector signal:

$$\dot{N}_i = K S_R \quad (5)$$

The measured evaporation flux was divided by the area of the deposit spot to determine the intensity of the evaporating gas. These measured intensities are also plotted in Fig. 10, curve 3. There appears to be fair agreement between the extrapolated vapor intensity curve and the measured vapor intensities. Two error flags are shown which represent the expected accuracy of the surface temperature measurement ($\pm 1^\circ\text{K}$) and the deposit spot area (± 10 percent). Within the accuracy of the measurements, the evaporation rate follows the experimental relation of Eq. (4) over this range of surface temperatures. As long as the deposit spot area was held constant and the surface temperature changed slowly, consistent and reproducible evaporation intensity measurements could be made while either warming or cooling the target surface. Since the deposit spot area would decrease with time as the condensate evaporated, it was difficult to make very precise measurements or calculations of deposit area. Within the indicated limits of accuracy, evaporation rates are easily measured over a range of surface temperatures for which evaporation rates could not be determined by other techniques.

4.2.3.2 Equilibrium Evaporation Rate

Several experiments were conducted to determine if the rate of evaporation into a vacuum at a given surface temperature is the same as the rate of evaporation when a beam is striking the surface with an intensity equal to the evaporation intensity. This is an equilibrium condition between rate of strike and rate of evaporation. If there is no coupling between the condensation and evaporation processes and the entire incident beam condenses on the target surface, then this equilibrium condition should occur at the surface temperatures measured previously for evaporation into a vacuum.

The equilibrium surface temperature was determined as described in Section III by condensing an incident beam on the target surface and then slowly warming the target surface until the gas intensity leaving the surface equaled the incident beam intensity. Several beam intensities were used, and the surface temperatures for this equilibrium condition are shown in Fig. 10. The data points are generally scattered about values slightly less than the temperatures on the curve for evaporation rate into a vacuum; however, once again the surface area of the deposit spot affects the results. Since it is generally impossible to generate a molecular beam with precisely the same diameter as the deposit spot, an error in the determination of the equilibrium intensity is introduced. The incident beam is generally of greater diameter than the condensate deposit spot. The approximate magnitude of this effect will be discussed in Section 4.3. It appears that the equilibrium evaporation rate and the evaporation rate into a vacuum differ at most by a small factor and may be equal.

4.2.4 Critical Supersaturation Ratio

With the evaporation rate experimentally determined, the data for intensities and surface temperatures to initiate condensation can be better analyzed. Referring to Fig. 10, the data for initiation of condensation and equilibrium between condensation and evaporation form two distinct curves. In terms of temperature, the surface must be cooled approximately 7°K below the equilibrium state temperature to initiate CO₂ condensation on the bare copper surface. In terms of intensity, for a given surface temperature the intensity ratio between the two curves is identical to a pressure ratio (Eq. 1)). Therefore, to initiate condensation on the bare copper surface at a given temperature, the gas pressure (beam intensity) must be greater than the vapor pressure by a factor equal to the ratio between values on the two curves. This ratio suggests a required supersaturation to initiate the condensation process. Such ratios, generally referred to as critical supersaturation ratios, have been experimentally measured for several metal vapors and chemical mixtures as reviewed in Refs. 18 through 20. This report deals with the first-known measurements of such phenomena for atmospheric gases. The experimentally determined critical supersaturation ratios for CO₂ are plotted in Fig. 11. It is noted that the critical supersaturation ratio decreases with increasing temperature in an exponential manner over the surface temperature range covered.

4.2.5 N₂ and Ar Data

A few experiments were conducted using N₂ and Ar beams to determine if the initiation of condensation followed the same trend as observed

for CO₂. In Fig. 12 curves are shown for the surface temperature and beam intensity relation for the initiation of condensation on a bare copper surface. For comparison, curves for evaporation intensity are shown which have been calculated from extrapolated vapor pressure curves (Ref. 17). It is apparent that a relation between intensity and surface temperature similar to that for CO₂ exists for the N₂ and Ar data. Also, a critical supersaturation ratio can be calculated from these curves as shown in Fig. 13. It is noted that the measured surface temperatures in these data may be quite inaccurate for quantitative analysis since the chromel-constantan thermocouples exhibit poor sensitivity in this range. However, it can be concluded that the observed phenomena for CO₂ condensation are not unique but are also exhibited by N₂ and Ar condensation and probably all atmospheric gases.

4.2.6 Theoretical and Experimental Comparisons

In 1916 Knudsen (Ref. 21) and Wood (Ref. 22) carried out experiments using metal vapor beams in which they observed a critical surface temperature above which condensation could not be initiated. Chariton and Simmenoff (Ref. 23), in similar experiments, observed a beam intensity dependence on the critical temperature for condensation. Motivated by this work, Frenkel (Ref. 24) developed a theory for condensation based on the heterogeneous nucleation of a vapor on a substrate material. Frenkel used the proposal of Langmuir (Ref. 25) that an atom which strikes a surface is not immediately reflected but stays on the surface for a finite time of adsorption which was derived by statistical methods:

$$\tau = \tau_0 \exp \frac{H_a}{k T_s} \quad (6)$$

The adsorbed atoms were considered to move about on the substrate and combine with other atoms to form centers of condensation for other atoms. Considering the rates of arrival and departure of atoms from the surface, Frenkel showed by statistical methods that the critical beam intensity for condensation was:

$$I_c = (4\sigma_a \tau_0)^{-1} \exp - \frac{H_v}{k T_s} \quad (7)$$

where H_v is the sum of the energy of adsorption of a single atom to the substrate and the dissociation energy of a pair of atoms which is the heat of vaporization of paired molecules. In later experimental studies such as those by Crockford (Ref. 26), Estermann (Ref. 27), and Yang, et al. (Ref. 28), the exponential relation between critical beam intensity and surface temperature was measured for several metal vapors over a wide range of surface temperatures.

The measurements for CO_2 , N_2 , and Ar beams reported herein clearly indicate that condensation of these atmospheric gases follows the form of Eq. (7), which was first used to describe the initiation of condensation of metal vapors. Figures 14 and 15 are a replot of the data of Figs. 10 and 12 showing the critical beam intensity for initiation of condensation as a function of reciprocal surface temperatures for CO_2 , N_2 , and Ar. The resulting straight lines in the semilog plots are in agreement with the prediction of Eq. (7). The data of Figs. 14 and 15 can also be used to evaluate the constants in Eq. (7) for the three gases:

$$(\text{CO}_2) I_c = 3.3 \times 10^{27} \exp - \frac{2300}{T_s} \quad (8)$$

$$(\text{N}_2) I_c = 1.6 \times 10^{27} \exp - \frac{620}{T_s} \quad (9)$$

$$(\text{Ar}) I_c = 1.8 \times 10^{26} \exp - \frac{680}{T_s} \quad (10)$$

These numerical values can in turn be used to calculate the heat term and period of oscillation term in Eq. (7) for comparison to published values. Table I gives the experimentally determined values of H_v and τ_o and published values of heats of vaporization and period of oscillation for adsorbed molecules (Refs. 29 and 30). Values for σ_o were calculated from published molecular diameters obtained by viscosity measurements (Ref. 29).

TABLE I
COMPARISON OF EXPERIMENTAL AND PUBLISHED VALUES

Experimental Values					Published Values		
Gas	T_s , 0K	σ_o , cm^2	H_v , cal/gm	τ_o , sec	T_s , 0K	H_v , cal/gm	τ_o , sec
CO_2	80	3.4×10^{-15}	103	1.9×10^{-14}	213	87.2	$10^{-13} - 10^{-14}$
N_2	22	3.1×10^{-15}	44	3.7×10^{-14}	78	47.6	$10^{-13} - 10^{-14}$
Ar	30	2.6×10^{-15}	34	3.3×10^{-13}	87	37.6	$10^{-13} - 10^{-14}$

The published data for periods of oscillation of adsorbed molecules generally fall in the range from 10^{-13} to 10^{-14} sec with very few precise measurements available. It is noted that for the N_2 and Ar data, a variation in surface temperature of 2°K would produce an order of magnitude change in the calculated τ_o . Since the precision of the surface temperature measurements for N_2 and Ar is about $\pm 2^\circ\text{K}$, the agreement with expected values of τ_o is considered good. Also, the calculated

heats of vaporization for N_2 and Ar are taken from the slope of curves determined by only four experimental points. Within the possible error of slope determination, a change in H_v of 5 cal/gram could be possible. The CO_2 data are more precise in both slope and absolute surface temperature measurements.

The existence of a critical supersaturation ratio between the gas pressure required to initiate condensation and the equilibrium vapor pressure at a given surface temperature had been reasoned in the early work by Gibbs (Ref. 31) and utilized by Frenkel (Ref. 32). By definition, the free energy is

$$F = U - TS + PV \quad (11)$$

A change in free energy is then:

$$dF = Vdp - SdT \quad (12)$$

If F_v and F_l are the free energies per molecule of the vapor and liquid phases, respectively, then for an isothermal process:

$$d(F_l - F_v) = (v - V)dp \quad (13)$$

Neglecting V with respect to v , Eq. (13) can be integrated as:

$$\Delta F_v = \int_{P_e}^{P_i} NkT \frac{dp}{p} \quad (14)$$

where the limits of integration are taken as the equilibrium pressure and incident beam pressure, or

$$\Delta F_v = \frac{RT}{v} \ln \left(\frac{P_i}{P_e} \right) \quad (15)$$

where ΔF_v is now in units of energy per unit volume. For the data analysis of this report, ΔF will be given in calories/cm³, T in °K, R will be taken as 1.98 calories/moles-°K, and P_i , the equivalent incident beam pressure, in dynes/cm². The specific volume v is determined by $v = M/\rho$ where M is the molecular weight and ρ is the density of the condensate. Equation (15) can also be written to express the critical condition for the initiation of condensation:

$$(\Delta F_v)_c = \frac{RT_c}{v} \ln \frac{P_c}{P_e} \quad (16)$$

where P_c/P_e is now the critical supersaturation ratio. As evidenced by Figs. 11 and 13, this exponential relation has been experimentally observed for CO_2 , N_2 , and Ar condensation. The density of condensed CO_2 was taken as 1.3 grams/cm³ (Ref. 33), whereas the densities of N_2 and Ar condensates were arbitrarily taken as 1.0 grams/cm³ since no density values in this temperature and pressure range are available.

Frenkel (Ref. 32) also derived an expression for the temperature difference between the equilibrium surface temperature and the temperature required to initiate condensation, which is the temperature difference between the curves of Figs. 10 and 12. For an isothermal process, the change in free energy can be related to the pressure change (Eq. (13)). Substituting Eq. (13) into the Clausius-Clapeyron relation in the form:

$$\frac{dp}{dT} = \frac{\Delta H_v}{T(v - v)} \quad (17)$$

leads to the relation

$$T_c - T_e = \frac{(\Delta F_v)_c(T_c)}{\Delta H_v} \quad (18)$$

Equation (16) has been used to determine the free energy of formation from the experimentally measured critical supersaturation ratios for CO_2 , N_2 , and Ar. Utilizing these calculated energies and the calculated heats of vaporization from Eq. (7) as shown in Table I, the temperature differences between initiation of condensation and the equilibrium temperature have been calculated from Eq. (18). These values are shown in Table II. Equation (1) has been used throughout to convert between beam intensity and pressure.

TABLE II
COMPARISON OF EXPERIMENTAL AND CALCULATED RESULTS

Gas	T_0 , °K	P_c , torr	P_c/P_e	$(\Delta F_v)_c$, cal/cm ³	$T_c - T_e$, °K Calculated, Eq. (18)	$T_c - T_e$, °K, Measured
CO_2	86	1.1×10^{-5}	9.5	11.3	7.2	6.4
	84	6.1×10^{-6}	11.8	12.1	7.6	6.8
	82	3.2×10^{-6}	15.0	13.0	7.9	7.6
	80	1.5×10^{-6}	19.5	13.9	8.3	7.7
	78	7.1×10^{-7}	25.0	14.7	8.5	7.9
N_2	23.5	4.7×10^{-6}	350	9.7	5.2	4.7
Ar	30	2.0×10^{-5}	29	5.0	4.4	4.0

The correlation between the calculated temperature differences and the measured temperature differences, the exponential relation observed for the critical intensity, and the agreement between measured and published constants for Eq. (7) indicate that the process for initiation of condensation of CO₂, N₂, and Ar gases can be described by Eqs. (7), (16), and (18).

One other possible correlation is suggested by the more recent theoretical work of Pound, Simnad, and Yang (Ref. 34), in which the basic model by Frenkel was extended to the development of a theoretical deposition rate of a molecular beam condensing on a surface. The assumptions of the theory are (1) every atom or molecule which strikes the surface comes to thermal equilibrium with the surface and is temporarily adsorbed, (2) the molecules move at random over the surface until they join a growing cluster of atoms, called an embryo, or leave the surface by evaporation, (3) the embryos are assumed to form uniformly over the substrate surface rather than only at preferred sites for nucleation, such as dislocations, cracks, and impurities, (4) there is a critical size for the embryos, and (5) embryos below this size will tend to evaporate and those above the critical size will tend to form a stable nucleus for nucleation.

Using the kinetic theory of gases, thermodynamical and statistical concepts, and random walk considerations, expressions are derived for the equilibrium concentration of adsorbed atoms or molecules, the free energy of formation of critical nuclei, and size of critical nuclei. The final result gives the deposition rate as a function of many factors:

$$I = [\gamma (\sin \theta) a_0 / 2mkv] [P_i^2 / -\Delta F_v T_s] \times \exp [(-2\Delta F_{ad} + \Delta F_d + \Delta F^*) / kT_s] \quad (19)$$

Because of the many unknowns, no direct experimental test of Eq. (19) is possible; however, a useful relation has been derived from it which relates the temperature dependence of critical supersaturation (Ref. 34). The standard free energy of formation ΔF^* of a critical nucleus is related to the bulk free energy per unit volume, ΔF_v .

$$\Delta F^* = 16\pi r^3 f(\theta) 3\Delta F_v \quad (20)$$

The free energy at the critical supersaturation condition, $(\Delta F_v)_c$, is in turn related to the critical supersaturation ratio (P_c / P_e) by Eq. (16). Using these relations, Eq. (19) has been altered to give the temperature dependence of the bulk free energy change per unit volume:

$$\frac{1}{(\Delta F_v)_c^2} = [3 kT_c (9 + \ln P_c) / 8\pi r^3 f(\theta)] - [3\Delta F_{ad} / 8\pi r^3 f(\theta)] \quad (21)$$

for the condition of critical supersaturation. Equation (21) predicts a straight line plot of $1/(\Delta F_v)_c^2$ versus $T_c(9 + \ln P_c)$. The experimental data for CO₂ have been plotted in this manner using the values of $(\Delta F_v)_c$ calculated from Eq. (16). The resulting curve is shown in Fig. 16. The data appear fairly linear except for the three points representing the lower surface temperatures, which are also the least accurate because of fewer data points taken for surface temperatures below 80°K.

A recent modification of this theory by Lothe and Pound (Ref. 35) resulted in a relationship in which a plot of $1/(\Delta F_v)_c^2$ versus $T_c(41 + \ln P_c)$ should produce a straight line. The CO₂ data were once again plotted for this relationship as shown in Fig. 17. Even though the linearity is somewhat better than in Fig. 16, it is felt that more data over a wider range of temperatures would be required to establish the validity of the relationship. The CO₂ data cover the range from 77 to 89°K.

The good correlations given by Eqs. (7) and (16), as well as the possible correlation of Eq. (19), suggest that the theoretical treatments of nucleation used to explain metal vapor depositions phenomena are applicable to the process of atmospheric gas condensation. Therefore, it is possible that other phenomena observed for metal vapor condensation may be associated with atmospheric gas condensation, such as:

1. Estermann (Ref. 27) observed that the critical temperature and pressure for the initiation of condensation depended on the beam width, which he attributed to the surface mobility of the atoms. In a separate beam experiment, he demonstrated migration of the surface atoms.
2. As discussed in the review of experimental data (Ref. 18), several experimenters have observed changes in the conditions for the initiation of condensation as the surface structure and level of contamination are varied.
3. The critical supersaturation ratio has been observed to increase as the number of lattice imperfections and surface cracks is decreased (Ref. 18).
4. For some metal vapor beam deposits, it has been observed that as the film thickens it develops a preferred orientation which is related to the angle of incidence of the beam (Ref. 18).
5. Sears and Cahn (Ref. 36) and Aziz and Scott (Ref. 37) have suggested possible effects caused by the energy level of the impinging molecules in the beam. No definitive experiments have been reported in this area, which is quite amenable to experimentation by molecular beam techniques.

4.3 CONDENSATION RATE EXPERIMENTS

4.3.1 Calculation of a Beam Capture Coefficient

Once the condensation process has been initiated on a bare copper surface, the reflected gas flux decreases with time if the surface temperature is further decreased, as shown in Figs. 8 and 9. Since the decrease in reflected gas flux is inversely proportional to the increase of condensed gas flux, the fraction of the incident beam condensing on a surface is given by:

$$C_b = 1 - \frac{\dot{N}_r}{\dot{N}_i} \quad (22)$$

where C_b is the beam capture coefficient. If any gas is evaporating from the target surface, the magnitude of the evaporation flux can be determined by shutting off the incident beam and recording the remaining detector signal. The reflected gas flux is then given by:

$$\dot{N}_r = \dot{N}_i - \dot{N}_v \quad (23)$$

As discussed in Section II, the detector signals are related to the gas flux by a previously determined calibration constant. Figures 18 and 19 are plots of the beam capture coefficient for the data in Figs. 8 and 9. Several experiments were conducted in an attempt to explain the observed temperature- and time-dependence curves for beam capture coefficient.

4.3.2 Temperature-Dependent Curves of Beam Condensation Rate

In the condensation rate experiments it was noted that as the surface temperature was lowered below the temperature at which condensation began, the diameter of the visible condensate deposit spot increased. The size of the deposit spot was also observed to increase with time when the surface temperature was held constant after the initiation of condensation. Then, for the data in Figs. 18 and 19, as the beam capture coefficient increased, the deposit spot size on the target increased. Since the initiation of condensation was shown to be a very sensitive function of beam intensity, it was suspected that some lower intensity portions of the incident beam were not beginning to condense at the same temperature as the higher intensity center portion and were being reflected by the target until the temperature was further decreased.

In the beam collimation process, a beam of constant intensity cross section is not generated but consists of a profile with a constant intensity portion at the center surrounded by a region of decreasing

intensity with increasing distance from the beam center. Using the skimmer and collimator sizes and the distance between them and the target, a trapezoidal beam profile can be calculated as shown in Fig. 20 and discussed in Ref. 38. For the beam chamber geometry used in these experiments, the beam center, referred to as the umbra, was a 4-mm-diam circle, and the region of decreasing intensity, referred to as the penumbra, was a region between the center 4-mm circle and an outer circle of 9-mm diameter. A few experiments were made to measure the actual beam profile in intensity by sweeping an ionization gage with a 0.5-mm orifice through the beam at a position between the collimator and target. The results are shown in Fig. 21.

In the early work by Estermann (Ref. 27), beam experiments with metal vapors were reported in which the umbra was observed to condense while the penumbra continued to be reflected. The measured beam profile (Fig. 21) and the intensity dependence for the initiation of condensation (Fig. 10) have been used to calculate a reflected flux variation with surface temperature. For a given intensity on the intensity profile (Fig. 21), the surface temperature required to initiate condensation at that intensity is determined from Fig. 10. The portion of the incident beam flux condensing on the target for the given intensity and temperature is then:

$$\Delta \dot{N}_c = C_i (\Delta I_i) (\Delta A) \quad (24)$$

where C_i is the capture coefficient for a given intensity, ΔI_i is the intensity at one point on the intensity profile, and ΔA is the increment of surface area for intensity ΔI_i . The reflected gas flux from the increment ΔA is then:

$$\Delta \dot{N}_r = \dot{N}_i - C_i (\Delta I_i) (\Delta A) \quad (25)$$

The total gas flux leaving the surface at a given surface temperature is determined by summing the increments of intensity times area over the beam profile from the maximum intensity down to the critical intensity below which condensation will not occur at the given surface temperature:

$$\dot{N}_t = \dot{N}_i - \sum_{r_o}^{r_c} C_i (\Delta I_i) (\Delta A) + \dot{N}_v \quad (26)$$

where \dot{N}_t is the total gas flux leaving the surface at a given temperature, \dot{N}_v is the evaporation flux at the given temperature, and the summation limits r_o and r_c represent the radius of the umbra and the critical radius beyond which the incident beam is not condensing.

Equation (26) was used to calculate the change in gas flux leaving the surface with C_i held constant for all intensities on the beam profile. The evaporation flux at any temperature was also determined from values in Fig. 10. Figure 22 is a plot of the calculations for three different values of C_i . The tabulated results using Eq. (26) are listed in Appendix IV. For comparison, several experimental data points are also shown.

Two important conclusions are suggested by the comparison between the calculated and experimental curves in Fig. 22. First, the apparent change in capture coefficient with surface temperature (Fig. 19) could be the result of the beam intensity profile, whereas the actual capture coefficient, C_i , is a constant value. Secondly, if the capture coefficient is a constant for all the intensities of the beam profile greater than the critical intensity, it must equal unity since this is the only value of C_i which produces a curve approaching the experimental limit of unity beam capture as the surface temperature is decreased (Fig. 19).

Several experiments were conducted in which the surface temperature was first decreased after initiation of condensation and then increased. During the temperature decreasing process, a visible condensate deposit would build up on the surface. As previously mentioned, the visible spot diameter increased as the surface temperature decreased. When the surface temperature was increased, the incident beam was then striking a previously deposited condensate spot and not a bare copper surface. Under these conditions, the incident beam continued to condense on the surface as the surface temperature was increased. Even when the surface temperature was increased to the critical temperature required to initiate condensation on a bare surface, the incident beam continued to condense as portrayed in Fig. 5 and discussed in Section III. As the surface temperature was increased further, the net process remained that of condensation until the equilibrium temperature was reached when the total flux leaving the surface equaled the incident beam flux. Even at temperatures above the equilibrium temperature, the incident beam readily condensed, even though the evaporation flux was greater than the incident beam flux (i. e., a net evaporation process).

Figures 23 and 24 are calculated values of total beam capture coefficient for an incident CO_2 beam striking a CO_2 condensate deposit spot. Figure 23 shows values of C_b approaching unity as the temperature is lowered and then remaining generally greater than 0.8 for temperatures up to the equilibrium temperature. Figure 24 shows values of C_b for a lower beam intensity which remain around 0.9 for temperatures above the equilibrium temperature.

As in the previously described data, the deposit spot diameter would vary as the surface temperature was varied, which in turn caused a variation in the amount of low intensity beam gas in the penumbra which would strike and be reflected by a bare copper surface. As shown in the calculations, using Eq. (26), the reflection of the low intensity gas in the penumbra could account for the difference between the measured values of C_b and a unity value. Therefore, it is concluded that the capture coefficient is greater than the measured values shown in Figs. 23 and 24 and possibly equal to unity. At the lower temperatures the value of C_b is actually measured to be quite near unity (>0.995). It is noted that the lower beam intensity data of Fig. 24 result in slightly higher values of capture coefficient. In this case, a larger fraction of the incident beam penumbra should consist of intensities below the measurable level of the detector system. A reduction in the detector signals would in turn cause an increase in the calculated capture coefficient. The effects of beam intensity on detector response are better exemplified by the data in the following section.

In order to further substantiate the effects of the beam intensity profile on the detector signals and calculated capture coefficients, an additional 4-mm collimator was installed between the existing chamber collimator and the target surface. This additional collimator would serve to reduce the dimensions of the penumbra, which in turn should reduce the quantity of gas which could be reflected from the bare copper surface surrounding the deposit spot. As shown in Fig. 25, this resulted in increased values of capture coefficient and also increased the temperature at which a unity value of capture coefficient was reached.

4.3.3 Time-Dependent Curves of Beam Condensation Rate

As previously mentioned and shown in Figs. 8 and 18, once the condensation process had been initiated, the surface temperature could be held constant, and the detector signal would decrease with time. At first it was suspected that this time dependence represented a required deposit thickness on the condensing surface before a steady-state condition could be maintained. However, as in the case of the temperature-dependent curves, it was observed that the visible deposit spot increased slightly with time during the deposition process. Since the calculated penumbra dimensions and measured profile dimensions of the incident beam were greater than the visible deposit spot diameter, it was suspected that the low intensity outer portions of the incident beam could be causing a change in detector signal as the deposit spot increased in size.

In order to explore this possibility, three types of experiments were conducted (1) an additional collimator was installed to reduce the penumbra, (2) several different beam intensities were used, and (3) several different surface temperatures were used at the same beam intensity. Figure 26 shows the change in detector signals resulting from use of an additional 4-mm collimator between the chamber wall collimator and the target surface. By reducing the diameter of the incident beam, the detector signal decreases more rapidly following the initiation of condensation than with the broader diameter beam.

When the incident beam intensity was reduced two orders of magnitude, the detector signal decreased much more rapidly to a zero value within 2 min (Fig. 26). At the lower beam intensity, much of the incident beam penumbra would be made up of intensities below the detectable level of the modulated beam detector. Therefore, any measureable effects of low intensity beam gas scattering from an uncoated portion of the target would be reduced, and a more rapid decrease in detector signal would be expected.

Figure 27 shows the effects of varying the surface temperature at which condensation is initiated on a bare surface. For the data points in the upper curve, the surface temperature was slightly below the critical temperature to initiate condensation. For the other data, the bare surface was first cooled to a temperature below the critical temperature, and then the incident beam was turned on. For the data taken at 58.5°K, there was no detectable signal when the beam was turned on. The large change in time response suggests that at the lower temperatures more of the lower intensity portions of the beam penumbra are able to condense, which reduces the reflected beam flux. At the lowest temperature, the total incident beam was apparently instantaneously condensed.

As in the case of the temperature-dependent curves, the time-dependent curves indicate that the measurement of condensation rate is affected by the incident beam intensity profile. Therefore, if there exists a required deposit thickness to produce a steady-state condensation rate, it cannot be differentiated from the effects caused by the incident beam intensity profile. However, the lower beam intensity data and lower surface temperature data suggest that the deposit buildup is quite small before the total incident beam is being condensed with unity capture coefficient.

4.3.4 Variations of Beam Angle of Incidence

Several beam condensation experiments were conducted at various angles of incidence from normal incidence to 80 deg as measured from the surface normal. The same temperature and intensity dependence was observed at high angles of incidence as indicated in Fig. 10. It is noted that, as the angle of incidence is increased, the incident beam is spread out over a larger portion of the target surface, which reduces the intensity per unit target area. However, as shown by the indicated points in Fig. 10, the initiation of condensation still obeys the same relation as that at normal incidence as long as the actual intensity per unit target area is used. Several condensation rate experiments were also conducted at various angles of incidence with the same results as discussed in the previous two sections for beams at normal incidence.

4.3.5 N₂ and Ar Condensation Rate

A few condensation rate experiments were conducted using N₂ and Ar beams. As shown in Fig. 28, the total incident beam capture coefficient followed the same trend with surface temperature as the CO₂ data. Based on these results, the mechanism for beam condensation of N₂ and Ar on a copper surface is the same as for the CO₂ beams.

4.3.6 Pressure-Temperature Regions for Condensation and Evaporation

Even though the beam intensity profile effects precluded the desired precision of capture coefficient measurement, the net process at the surface in terms of condensation or evaporation can be described in terms of gas pressure and surface temperature regions. Throughout some regions the capture coefficient appears well defined, whereas in others its probable value, or at least its limits, is suggested. The experimental data indicate that once condensation has been initiated at a surface interface, the capture coefficient approaches or equals a value of unity. The net process at the surface is then condensation. If the surface is cooled below the critical temperature to initiate condensation, the net process clearly remains condensation, and the capture coefficient remains very near or equal to unity. It is noted that a decrease in surface temperature below the critical temperature while holding a constant beam intensity can also be interpreted as an increase in the intensity or pressure supersaturation ratio, since a decrease in temperature is accompanied by a decrease in equilibrium pressure. Therefore, it can be concluded that for values of gas pressure and surface temperature falling above the critical supersaturation line, the net process at a

surface is condensation, and the capture coefficient takes on a near, or equal to, unity value. The data in Fig. 10 have been used to construct Fig. 29 with the beam intensity converted to equivalent gas pressure and the regions of condensation and evaporation indicated.

If the surface temperature is increased above the critical temperature following the initiation of condensation, it was observed that the net process remained condensation until the equilibrium temperature was reached and the condensing flux equaled the evaporating flux. The capture coefficient was also noted to generally remain greater than 0.8, as shown in Figs. 23 and 24, but the probable effect of the low intensity outer portions of the incident beam profile scattering from uncoated portions of the target surface has prevented precise measurements. As shown in the beam profile measurements and calculations, Fig. 22 and Appendix IV, the beam intensity profile effects could account for a difference between a measured value of 0.8 and an actual capture coefficient of 1.0. Therefore, it is indicated that the capture coefficient is greater than 0.8 and possibly equal to 1.0 between the critical supersaturation curve and the equilibrium curve, as indicated in Fig. 29.

As the temperature is increased above the equilibrium temperature, the net process changes from condensation to evaporation. Once again the incident beam gas readily condenses, even though the evaporation flux is greater than the condensation flux. As indicated by the data in Fig. 24, there is no apparent decrease in the capture coefficient value as the equilibrium temperature is exceeded. Measurements in this region were limited to temperatures below about 95°K since the evaporation flux would increase to values sufficiently large to saturate the mass spectrometer used in the modulated beam detector system.

SECTION V CONCLUSIONS AND SUGGESTIONS

The molecular beam experiments of the condensation and evaporation processes for CO₂, N₂, and Ar on cryogenically cooled copper surfaces at vacuum conditions can be summarized as follows:

1. The molecular beam technique has been established as a means for detailed and precise measurements of gas condensation and evaporation phenomena.
2. The scattering patterns of room temperature CO₂ beams from polished copper surfaces at and below room temperature follow

the classical cosine law for all beam angles of incidence between 0 and 80 deg. Also, the evaporation flux spatial distribution pattern from a spot of gas condensate follows the cosine law.

3. The initiation of condensation of CO₂, N₂, and Ar gases on cryogenically cooled copper surfaces follows a definite gas pressure and surface temperature relation which is predicted by the theoretical relation derived by Frenkel (Ref. 24). The existence of a critical supersaturation ratio for the initiation of condensation of CO₂, N₂, and Ar gases is well established. The experimentally determined ratios are in good agreement with the predictions of the classical thermodynamical relation which relates the critical supersaturation ratio to a free energy of formation. Also, the experimentally determined free energies of formation suggest a possible correlation with theoretically derived condensation rate equations (Ref. 34).
4. The measured CO₂ evaporation rate between 75 and 95°K is in agreement with the extrapolation from values published for higher temperatures.
5. The measurements of total beam capture coefficients are affected by the incident beam intensity profile, which prevents the direct measurement of the capture coefficient at a single intensity. However, for pressure ratios equal to or greater than the critical pressure ratio, the capture coefficient is equal to, or approaching closely, a unity value. For gas impingement on a previously deposited condensate at values of pressure ratio less than the critical supersaturation ratio, the capture coefficient remains greater than zero, but possible beam intensity profile effects preclude precise measurements.
6. For practical engineering applications, Fig. 29 can be used to determine the relative magnitudes of gas flux striking and leaving a condensate-covered surface as well as the pressure-temperature requirements to initiate condensation.

The results of these experiments together with the theoretical correlations suggest certain future experiments which should extend the present knowledge of the heterogeneous condensation process.

1. The theoretical treatments referred to in this report assume the condensation process to be independent of the incident gas energy. Molecular beams of higher energies can be used to readily determine the extent of applicability of this assumption.

2. If a means of controlling the effects of the incident beam intensity profile can be developed, the magniture of the capture coefficient for a single beam intensity can be determined, as well as its value over a wide range of pressures relative to the vapor pressure.
3. In several of the referenced articles, changes in the critical supersaturation ratio were observed as a function of the surface structure and nature of adsorbed gases. Since such changes could have significant bearing on the applicability of cryogenically cooled surfaces for vacuum pumping, molecular beam experiments are suggested in which the surface structure and composition are carefully controlled.
4. A complete understanding of the condensation process will also include knowledge of the molecular structure of the cryodeposits. Therefore, experiments are needed which can reveal the resulting crystalline or amorphous nature of the cryodeposits.

REFERENCES

1. Wang, E. S. J., Collins, J. A., Jr., and Haygood, J. D. "General Cryopumping Study." Advances in Cryogenic Engineering, Vol. 7, K. D. Timmerhaus (Ed.), Plenum Press, Inc., New York, 1962.
2. Wang, E. S. J., Collins, J. A., Jr., and Haygood, J. D. "Cryopumping in the Near Free-Molecule Flow Region." Advances in Cryogenic Engineering, Vol. 7, K. D. Timmerhaus (Ed.), Plenum Press, Inc., New York, 1962.
3. Dawson, J. P. "Cryopumping Capture Coefficients of Two Nitrogen-Oxygen Gas Mixtures." AEDC-TDR-64-150 (AD603623), August 1964.
4. Brown, R. F. "Cryopumping of Nitrous Oxide." AEDC-TDR-63-267 (AD431229), February 1967.
5. Barnes, C. B. and Hood, C. B. "Correlation between Pumping Speed & Cryoplate Geometry." Advances in Cryogenic Engineering, Vol. 7, K. D. Timmerhaus (Ed.), Plenum Press, Inc., New York, 1962.
6. Chubb, J. N. and Pollard, I. E. "Experimental Studies of Hydrogen Condensation on to Liquid Helium Cooled Surfaces." Vacuum, Vol. 15, October 1965, p. 491.

7. Freeman, R. M. "In-Chamber Vacuum Gage Calibration Method and Its Application to Cryopumping Measurements." AEDC-TR-66-234 (AD645509), January 1967.
8. Moody, T. L. "Capture Coefficient of 300°K CO₂ on a 77°K Surface as Measured by the Rotating Gage Technique." AEDC-TR-66-231 (AD645510), January 1967.
9. Bagrow, N. N., Butenko, A. M., Guslyakow, A. A., Kulik, I. O., and Udovenko, V. F. "Operation of a Cryogenic Pump in the Free-Molecular Mode." Soviet Physics - Technical Physics, Vol. 12, No. 6, December 1967, p. 795.
10. Dawson, J. P. and Haygood, J. D. "Temperature Effects on the Capture Coefficient of CO₂." AEDC-TDR-63-251 (AD428497), January 1964.
11. Dawson, J. P. and Haygood, J. D. "Cryopumping." Cryogenics, Vol. 5, April 1965, p. 57.
12. Brown, R. F. and Heald, J. H., Jr. "Description and Performance of a Molecular Beam Chamber Used for Cryopumping and Adsorption Pumping Studies." AEDC-TR-66-135 (AD641388), October 1966.
13. Heald, J. H., Jr. "Performance of a Mass Spectrometric Modulated Beam Detector for Gas-Surface Interaction Measurements." AEDC-TR-67-35 (AD648984), March 1967.
14. Stickney, R. E. "A Discussion of Energy and Momentum Transfer in Gas-Surface Interactions." AEDC-TR-66-13 (AD630522), February 1966.
15. Knudsen, M. Annalen der Physik, Vol. 48, 1915, p. 1113.
16. Wood, R. W. Philosophical Magazine and Journal of Science, Vol. 30, 1915, p. 300 and Vol. 32, 1916, p. 364.
17. Dushman, S. Scientific Foundations of Vacuum Technique. (Second Edition). John Wiley & Sons, Inc., New York, 1962.
18. Hirth, J. P. and Pound, G. M. "Condensation and Evaporation of Solids." Progress in Materials Science, Vol. 11, Pergamon Press, 1963.
19. Wexler, S. "Deposition of Atomic Beams." Reviews of Modern Physics, Vol. 30, April 1958, p. 402.
20. Ehrlich, G. "Atomic Processes at Solid Surfaces." Annual Review of Physical Chemistry, Vol. 17 (H. Eyring, Ed.), Annual Reviews, Inc., Palo Alto, California, 1966, pp. 295-322.

21. Knudsen, M. Annalen der Physik, Vol. 50, 1916, p. 472.
22. Wood, R. W. Philosophical Magazine and Journal of Science, Vol. 30, 1915, p. 300 and Vol. 32, 1916, p. 314.
23. Chariton, C. and Simmenoff, M. Zit Physik, Vol. 25, 1924, p. 25.
24. Frenkel, J. Zit Physik, Vol. 26, 1924, p. 117.
25. Langmuir, I. The Physical Review, Vol. 8, 1916, p. 149.
26. Crockford, J. D. Proceedings of the Royal Society. London, 1923, p. 293.
27. Estermann, I. Zit Physik, Vol. 33, 1925, p. 320 and Zit Elektrochem, Vol. 31, 1925, p. 441.
28. Yang, L., Birchenall, C. E., Pound, G. M., and Simnad, M. T. "Some Observations on Heterogeneous Nucleation of Sodium Crystals from Atomic Beams." Acta Metallurgica, Vol. 2, May 1954, p. 462.
29. Handbook of Chemistry and Physics. The Chemical Rubber Publishing Co., Cleveland, Ohio, 1960. (42nd Edition.)
30. deBoer, J. H. The Dynamical Character of Adsorption. Oxford University Press, London, England, 1953.
31. The Collected Works of J. Willard Gibbs. Vol. I, Yale University Press, 1957.
32. Frenkel, J. Kinetic Theory of Liquids, Dover Publications, Inc., New York, 1955.
33. Tempelmeyer, K. E., Wood, B. E., and Mills, D. W., Jr. "In Situ Measurements of Thickness and Other Properties of Carbon Dioxide Cryodeposits by Optical Techniques." AEDC-TR-67-226 (AD662869), December 1967.
34. Pound, G. M., Simnad, M. T., and Yang, L. "Heterogeneous Nucleation of Crystals from Vapor." Journal of Chemical Physics, Vol. 22, July 1954, p. 1215.
35. Lothe, J. and Pound, G. M. "Reconsiderations of Nucleation Theory." Journal of Chemical Physics, Vol. 36, April 1962, p. 2080.
36. Sears, G. W. and Cahn, J. W. "Interaction of Condensable Gases with Cold Surfaces." Journal of Chemical Physics, Vol. 33, August 1960, p. 494.

37. Aziz, R. A. and Scott, G. P. "The Effect of Incident Atomic Velocity on the Structure of Evaporated Silver Films." Canadian Journal of Physics, Vol. 34, August 1956, p. 731.
38. Ramsey, N. F. Molecular Beams. Oxford University Press, London, England, 1956.

APPENDIXES

- I. ILLUSTRATIONS**
- II. CALCULATION OF MOLECULAR BEAM PRESSURE
FROM BEAM INTENSITY**
- III. CALCULATION OF DETECTOR CHOPPER WHEEL
EFFECTS ON SCATTERED BEAM SPATIAL DIS-
TRIBUTION PATTERNS**
- IV. CALCULATION OF BEAM INTENSITY PROFILE
EFFECTS ON REFLECTED GAS FLUX**

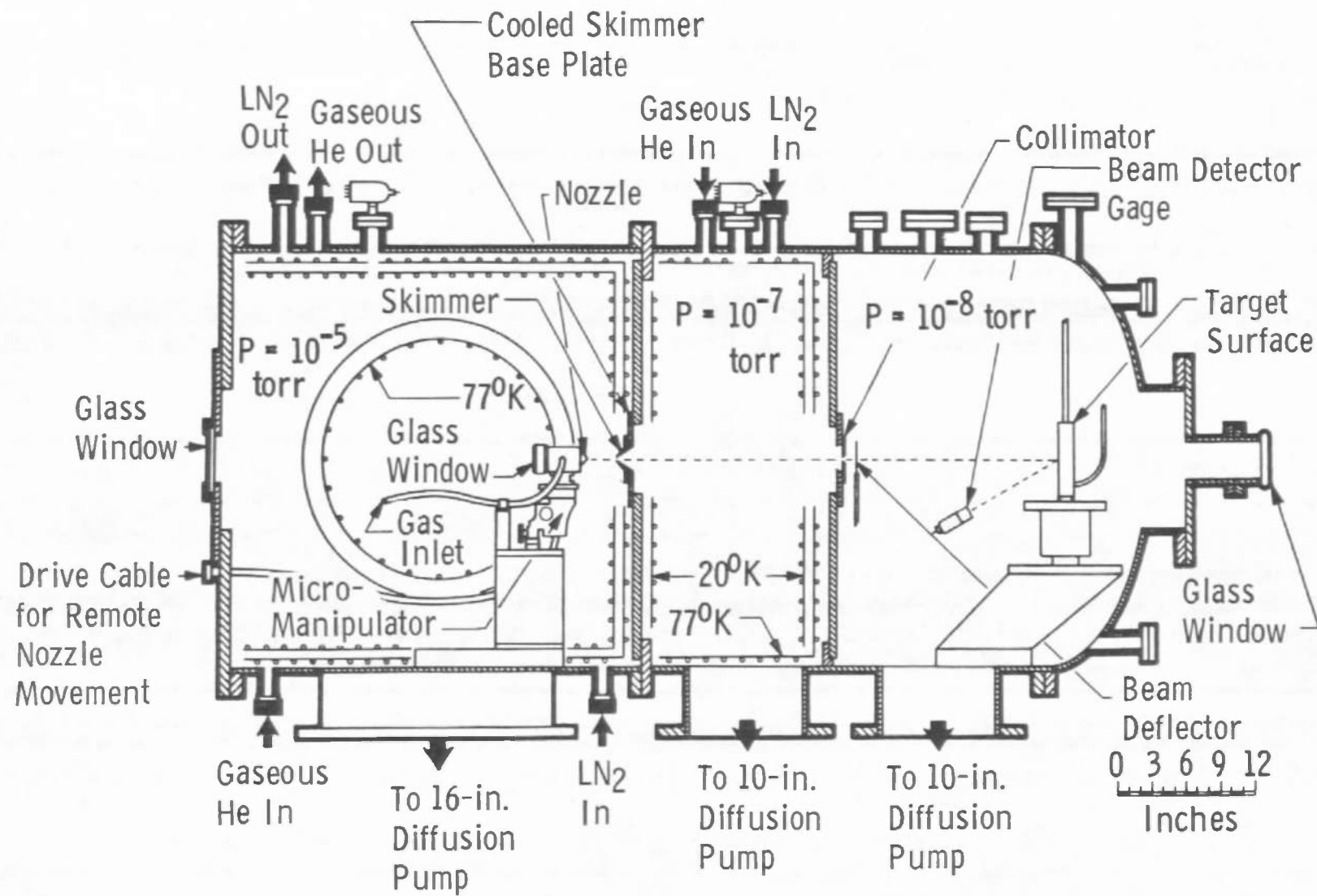


Fig. 1 Schematic of the AEDC Aerodynamic Molecular Beam Chamber

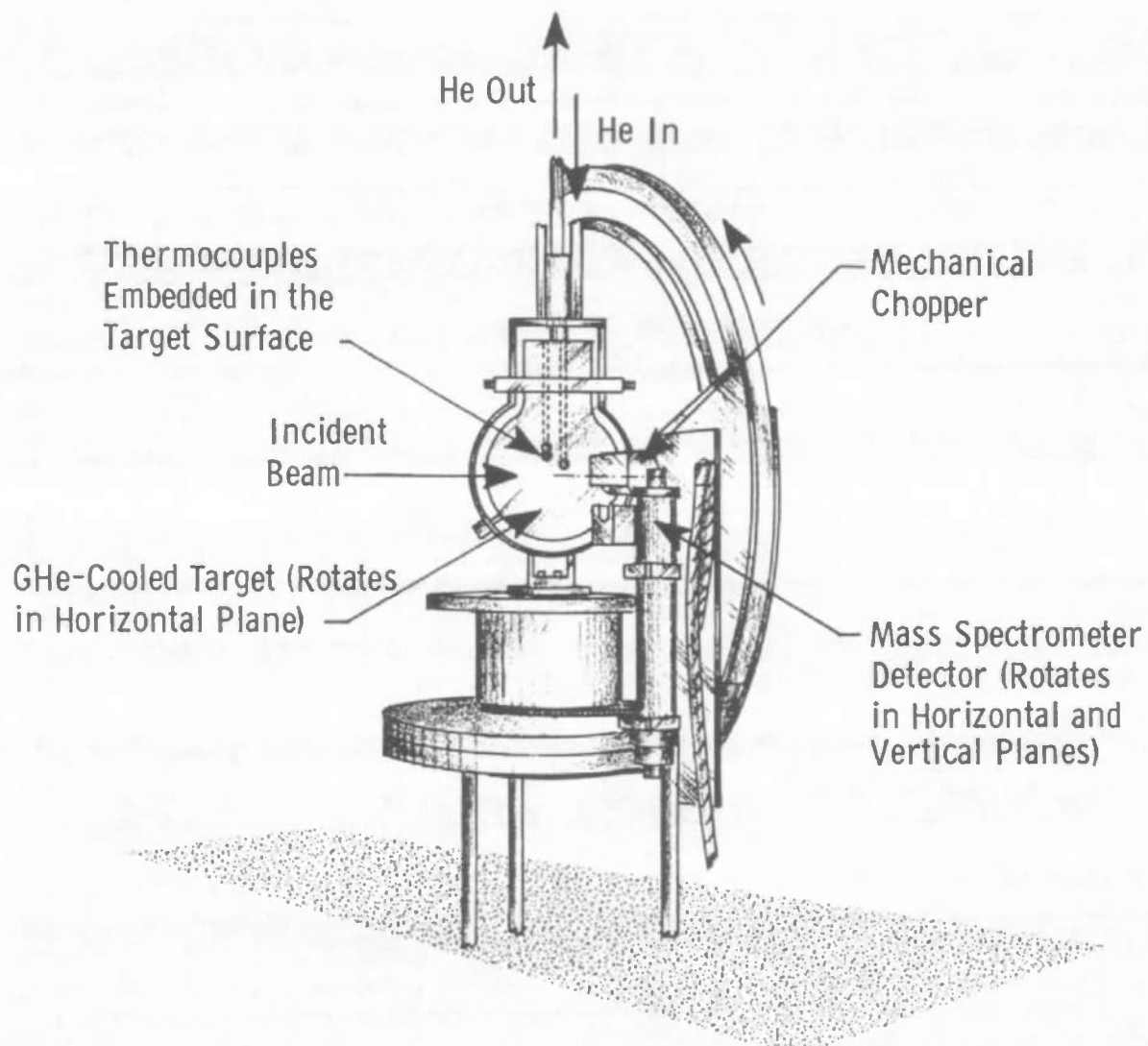


Fig. 2 Target and Mass Spectrometer Arrangement

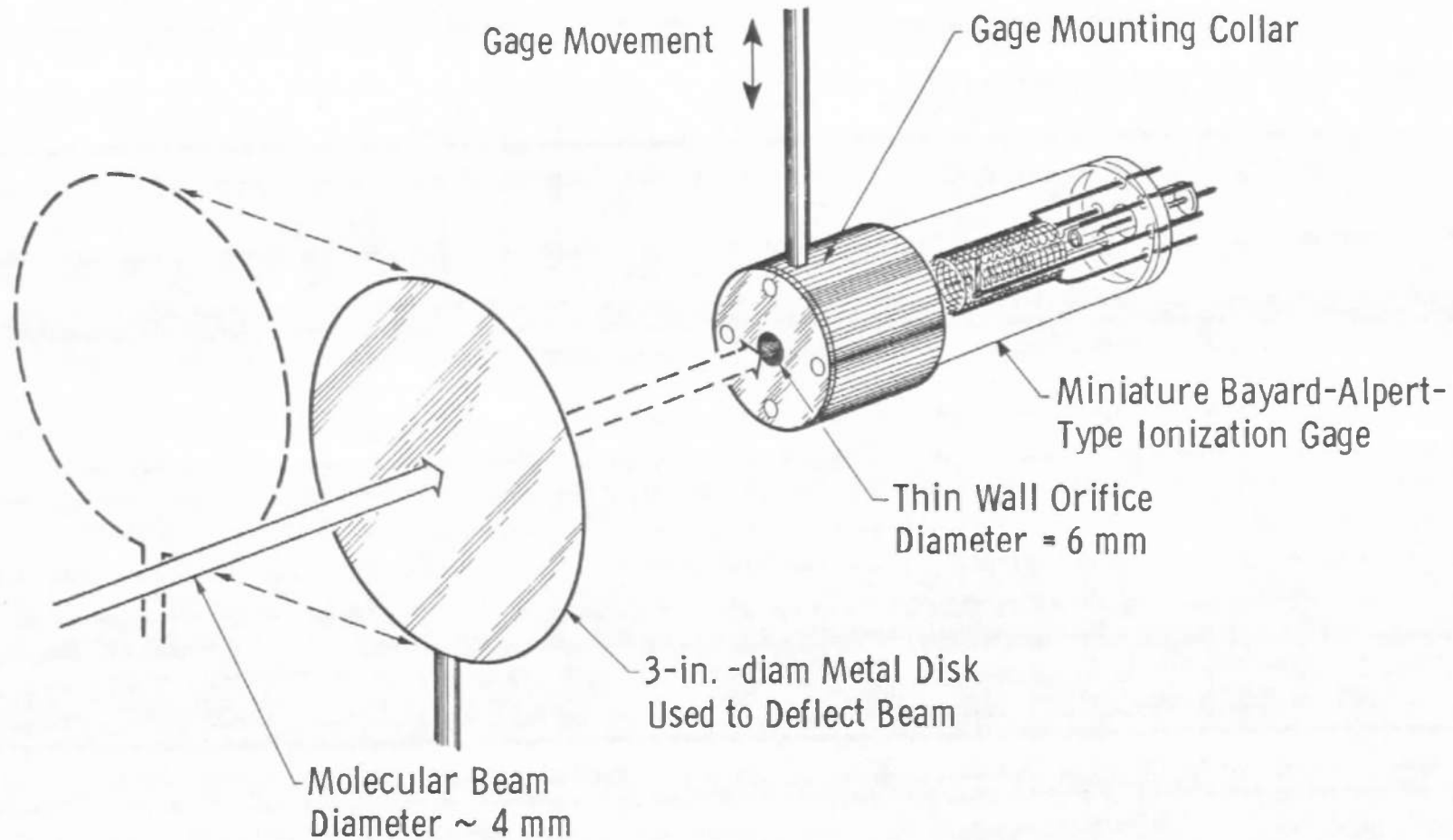


Fig. 3 Ion Gage Used to Measure Incident Beam Intensity

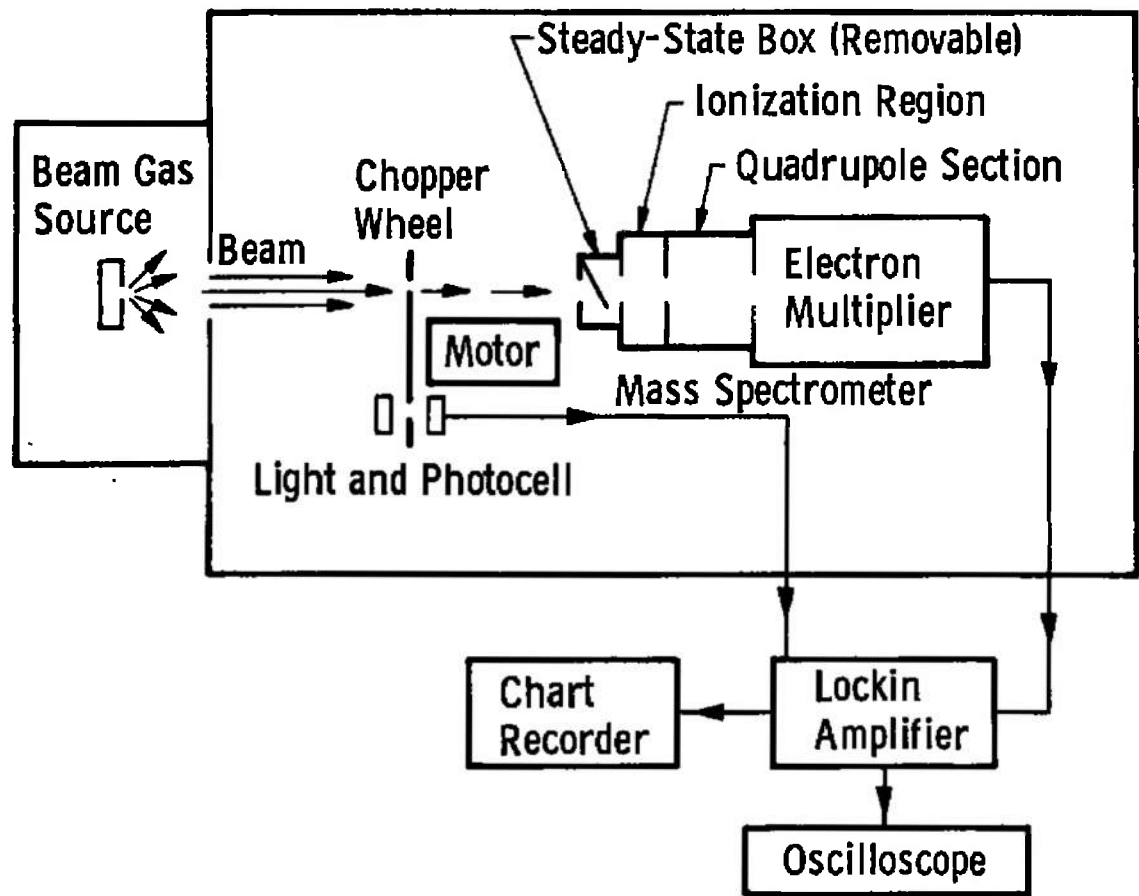


Fig. 4 Schematic of Mass Spectrometric Modulated Beam Detector

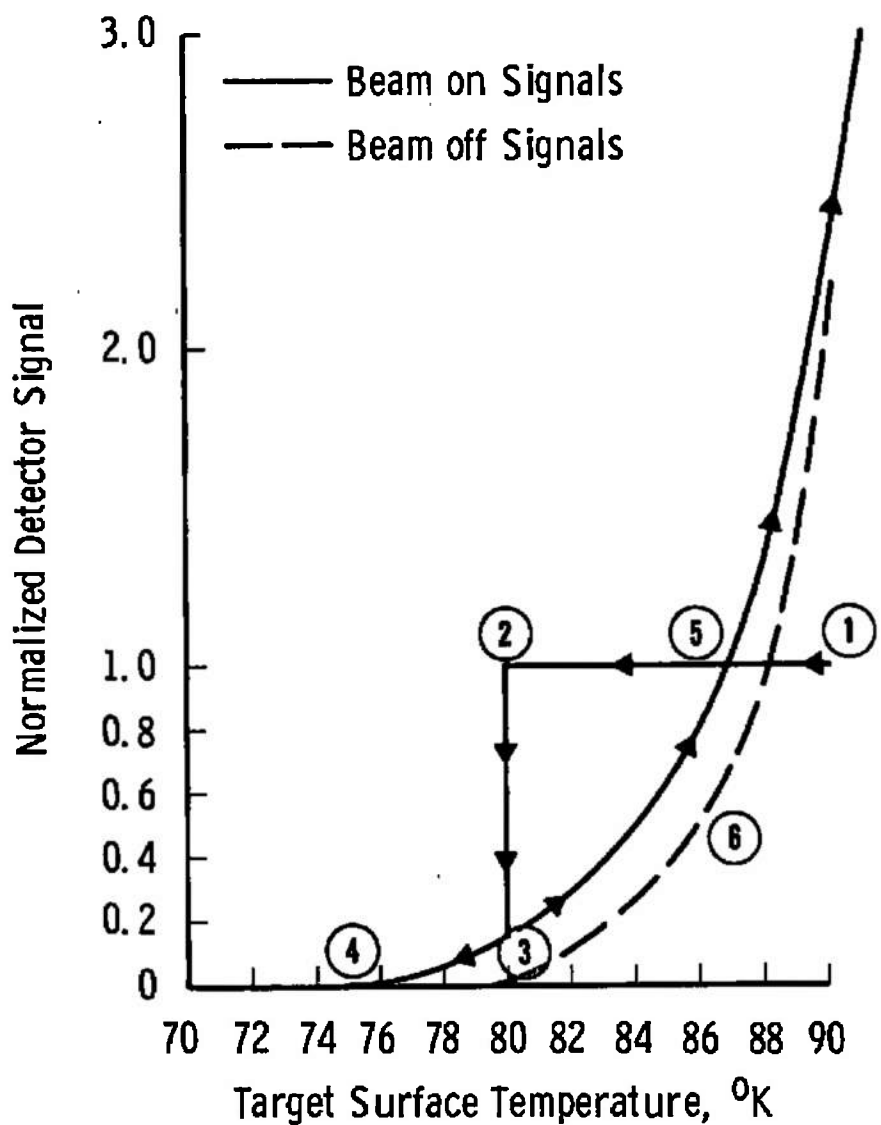


Fig. 5 Typical Condensation and Evaporation Experiment

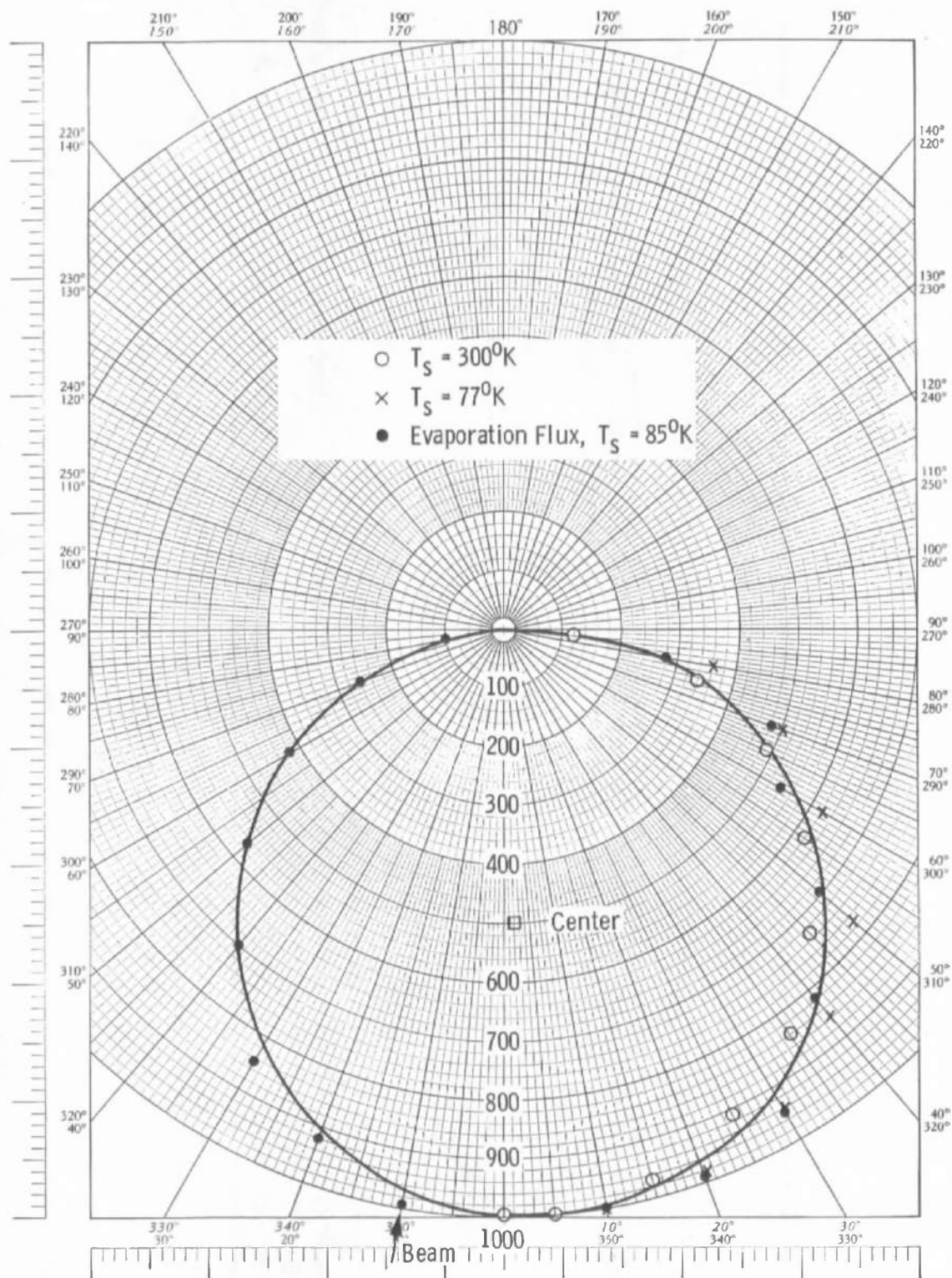


Fig. 6 Scattering Patterns at Near-Normal Incidence and Evaporation Flux Pattern

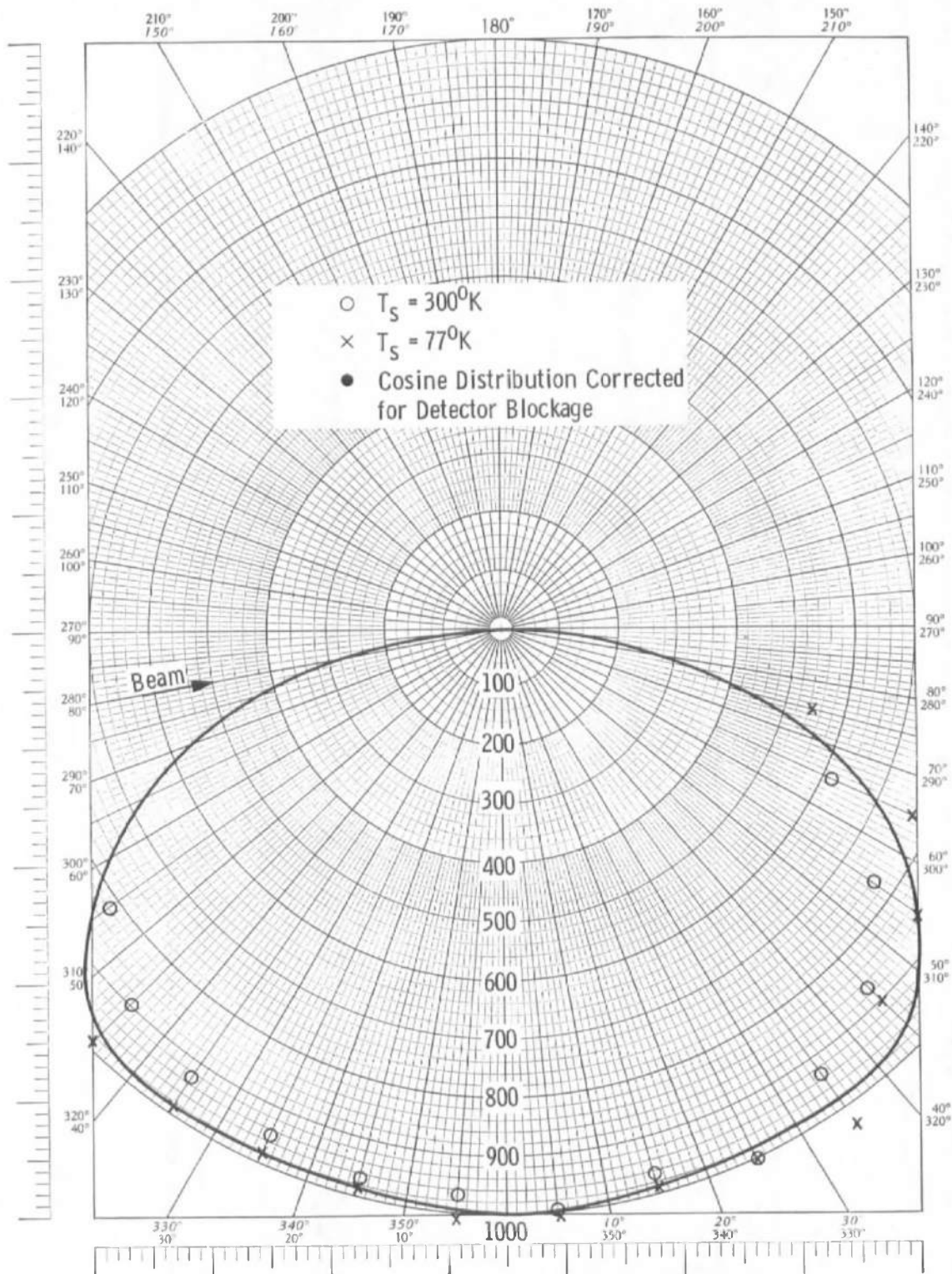


Fig. 7 Scattering Patterns at 80-deg Incidence

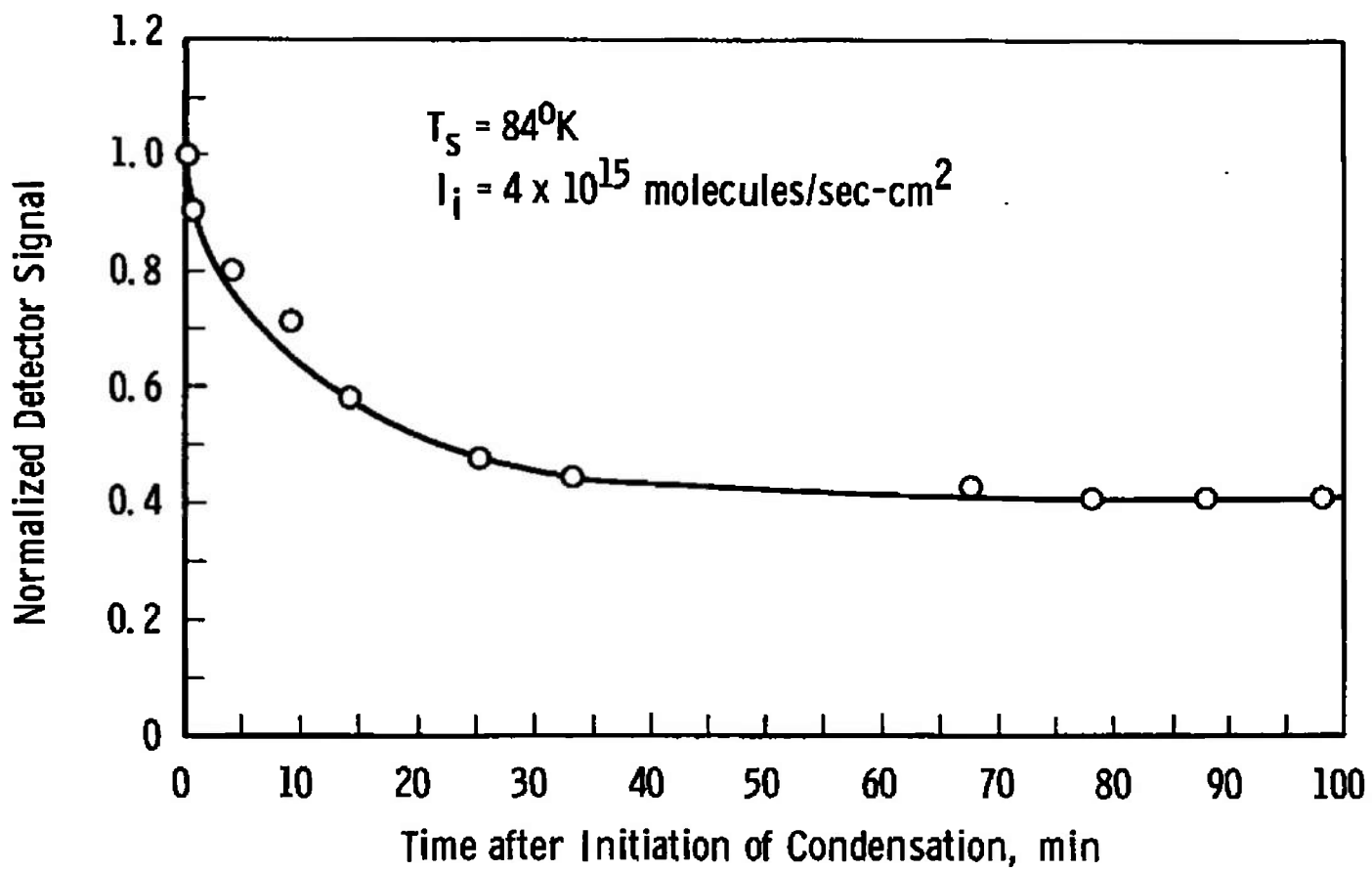


Fig. 8 Reflected Beam Signal versus Time after Initiation of Condensation

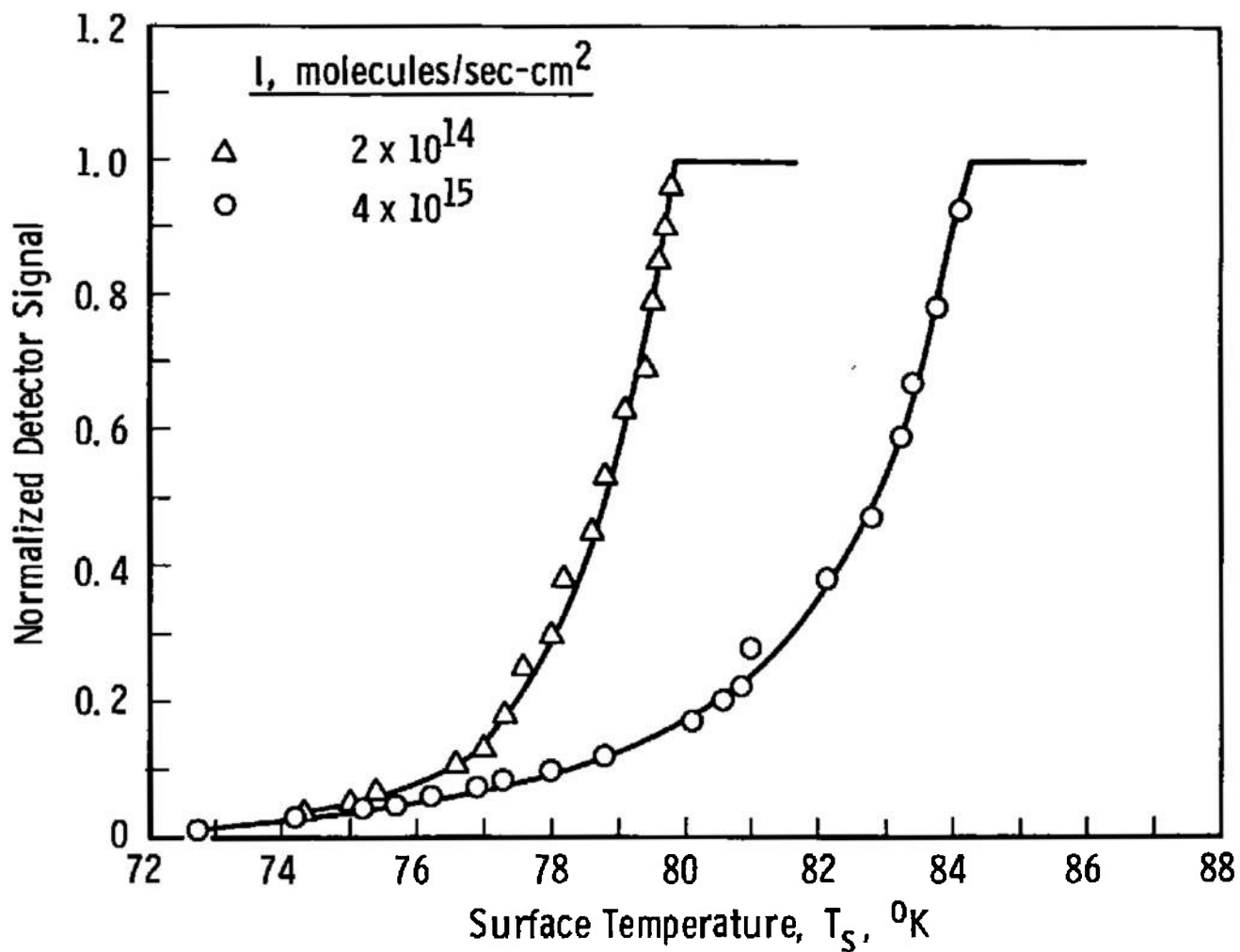
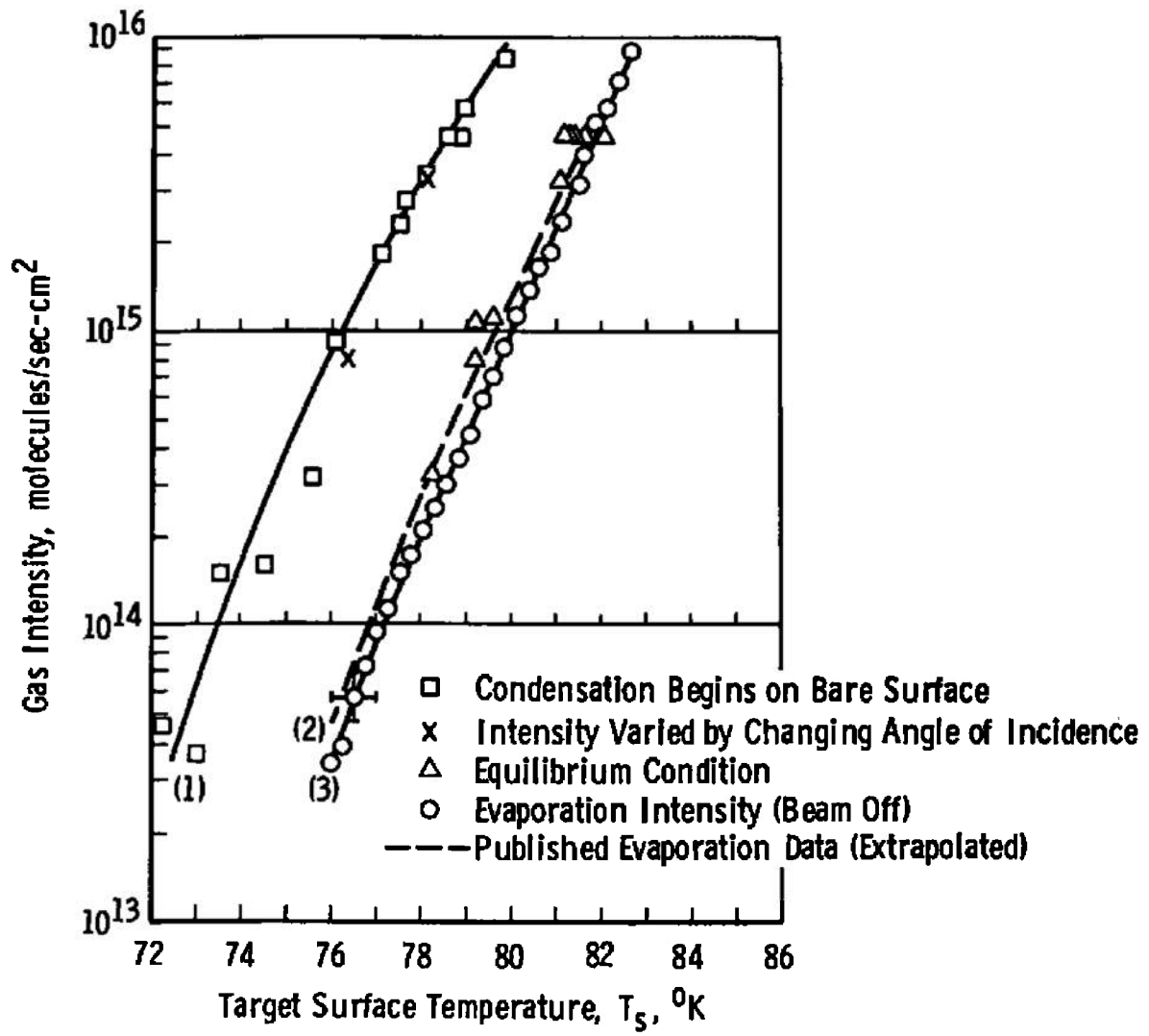


Fig. 9 Reflected Beam Signal versus Surface Temperature after Initiation of Condensation for CO₂

Fig. 10 Characteristic Curves of CO_2 Condensation and Evaporation

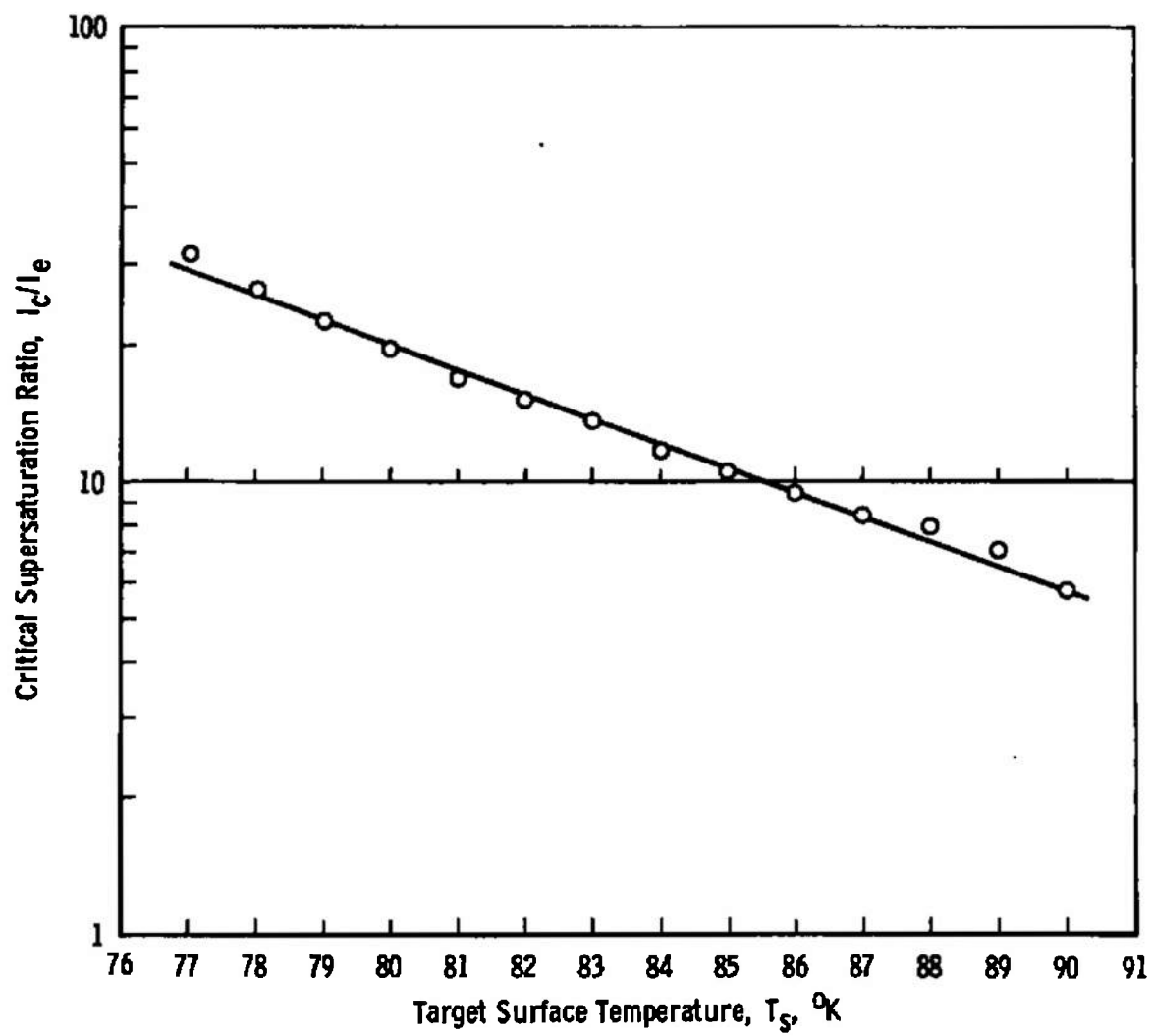
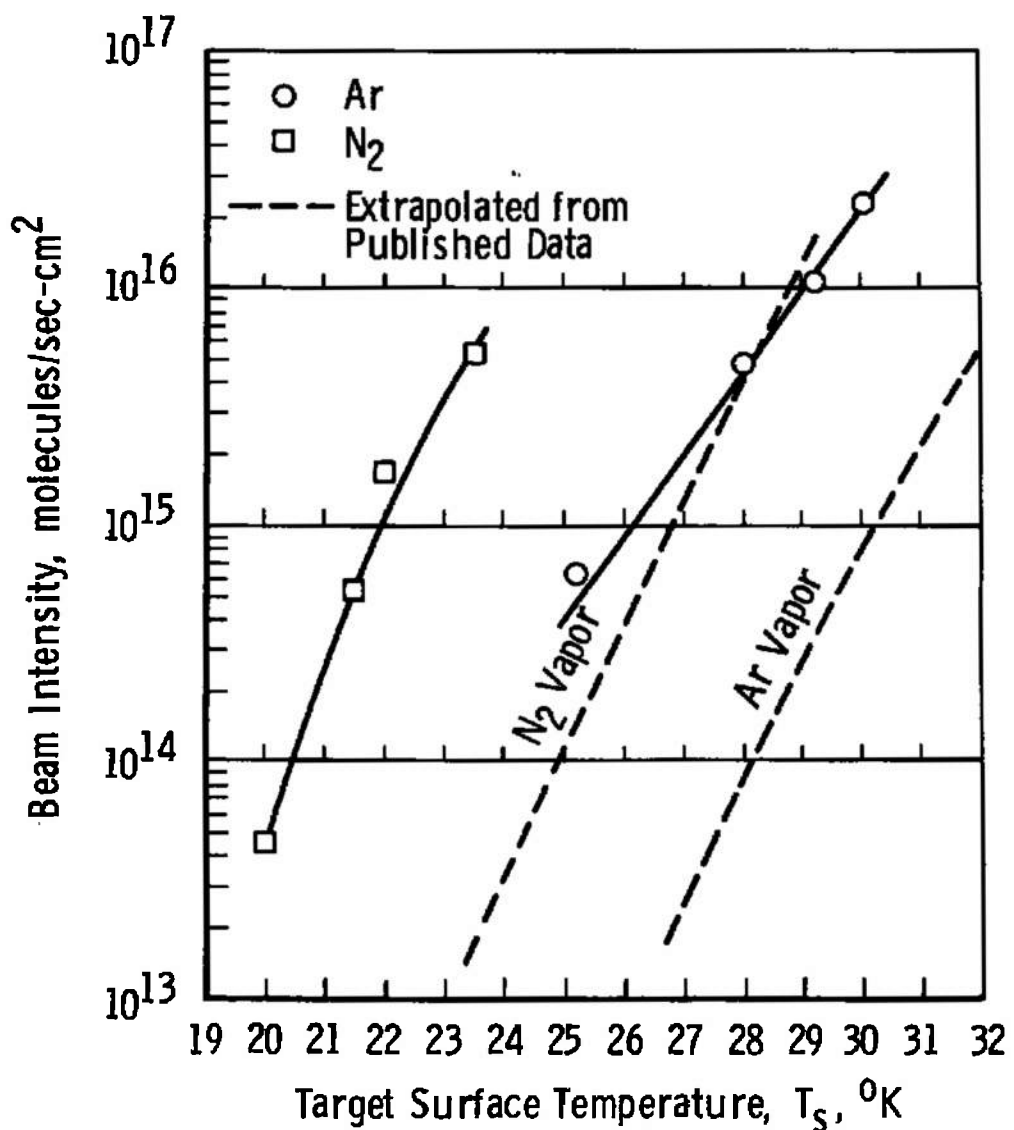


Fig. 11 Critical Supersaturation Ratios of CO_2

Fig. 12 Characteristic Curves of N₂ and Ar Condensation

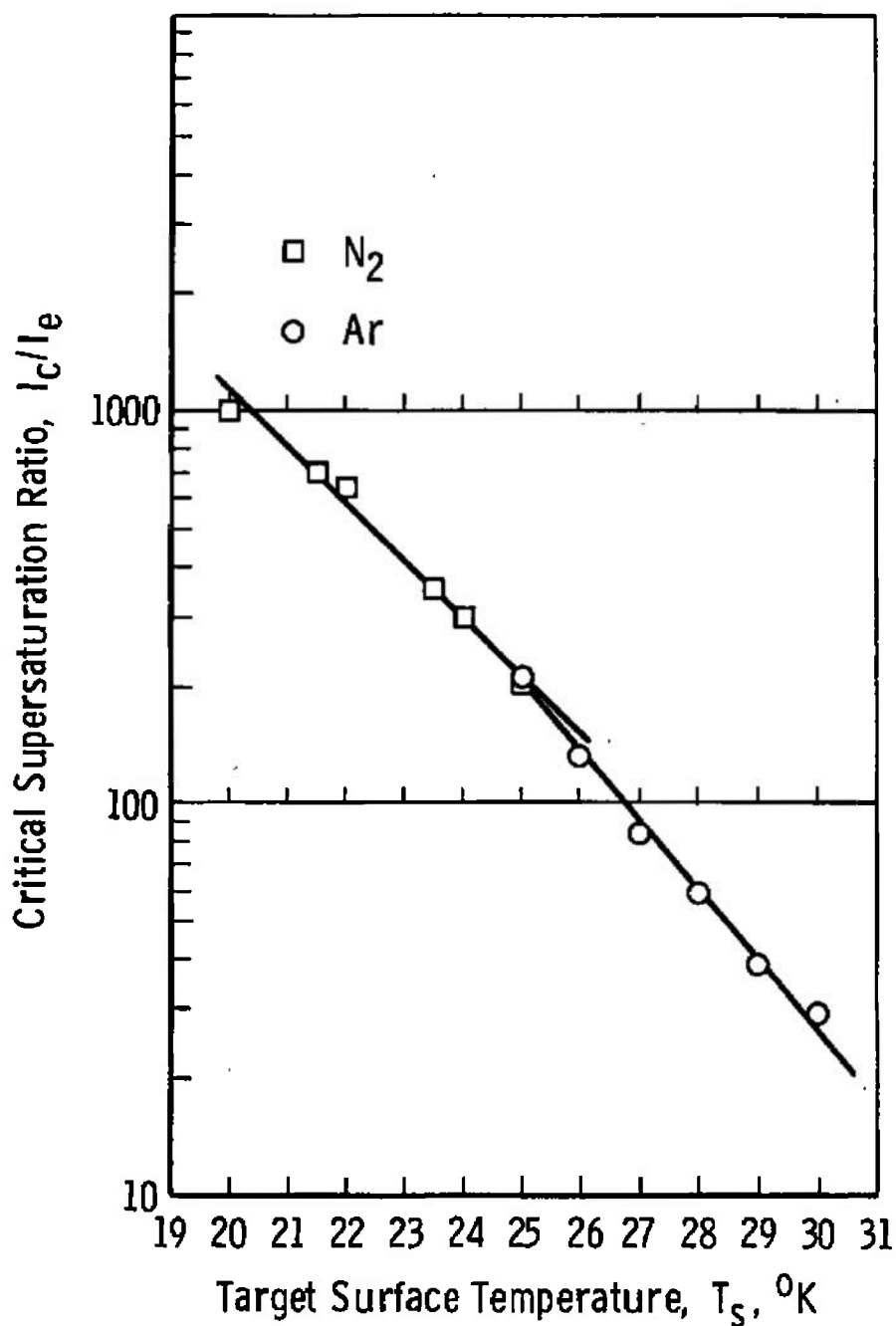
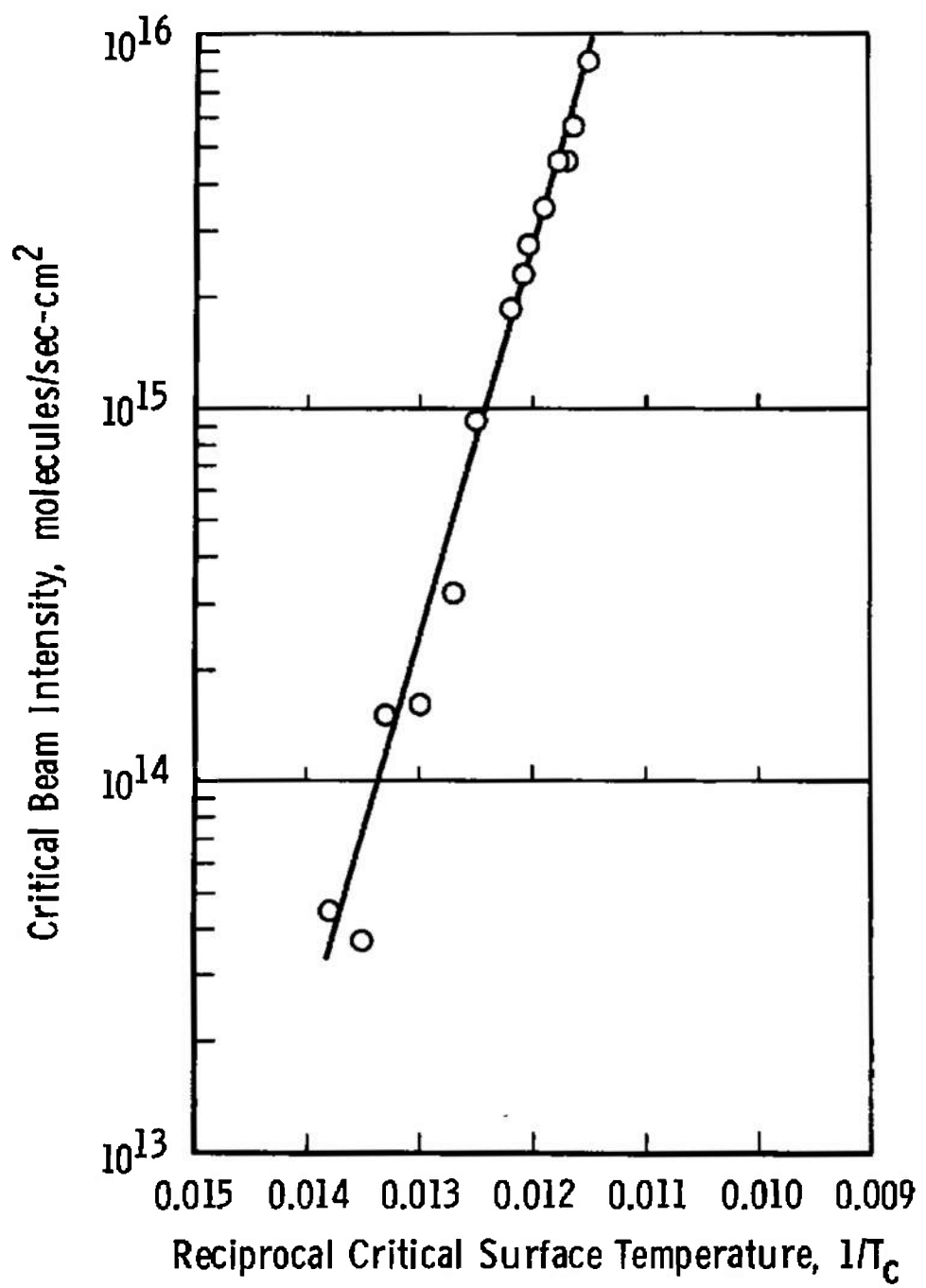
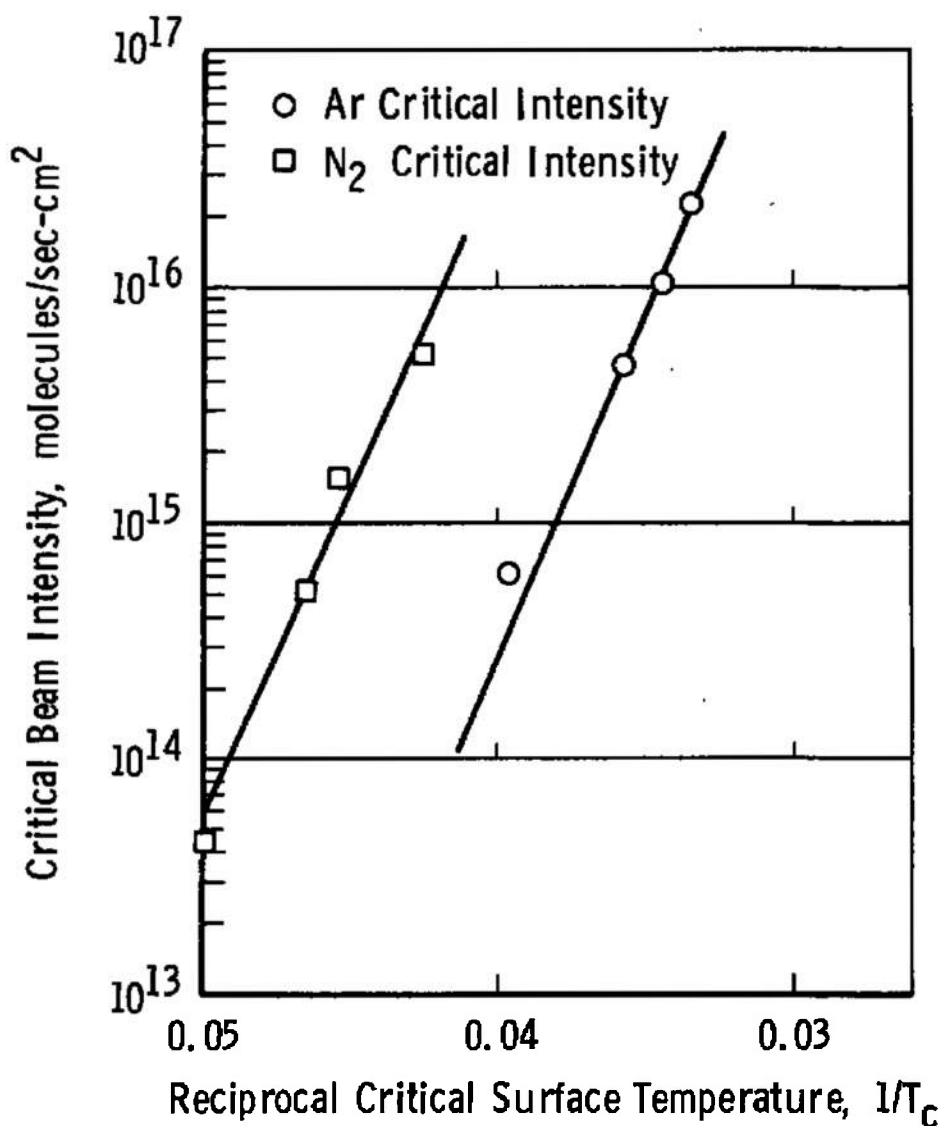


Fig. 13 Critical Supersaturation Ratios of N_2 and Ar

Fig. 14 Critical Intensity of CO₂ for Condensation

Fig. 15 Critical Intensity of N₂ and Ar Condensation

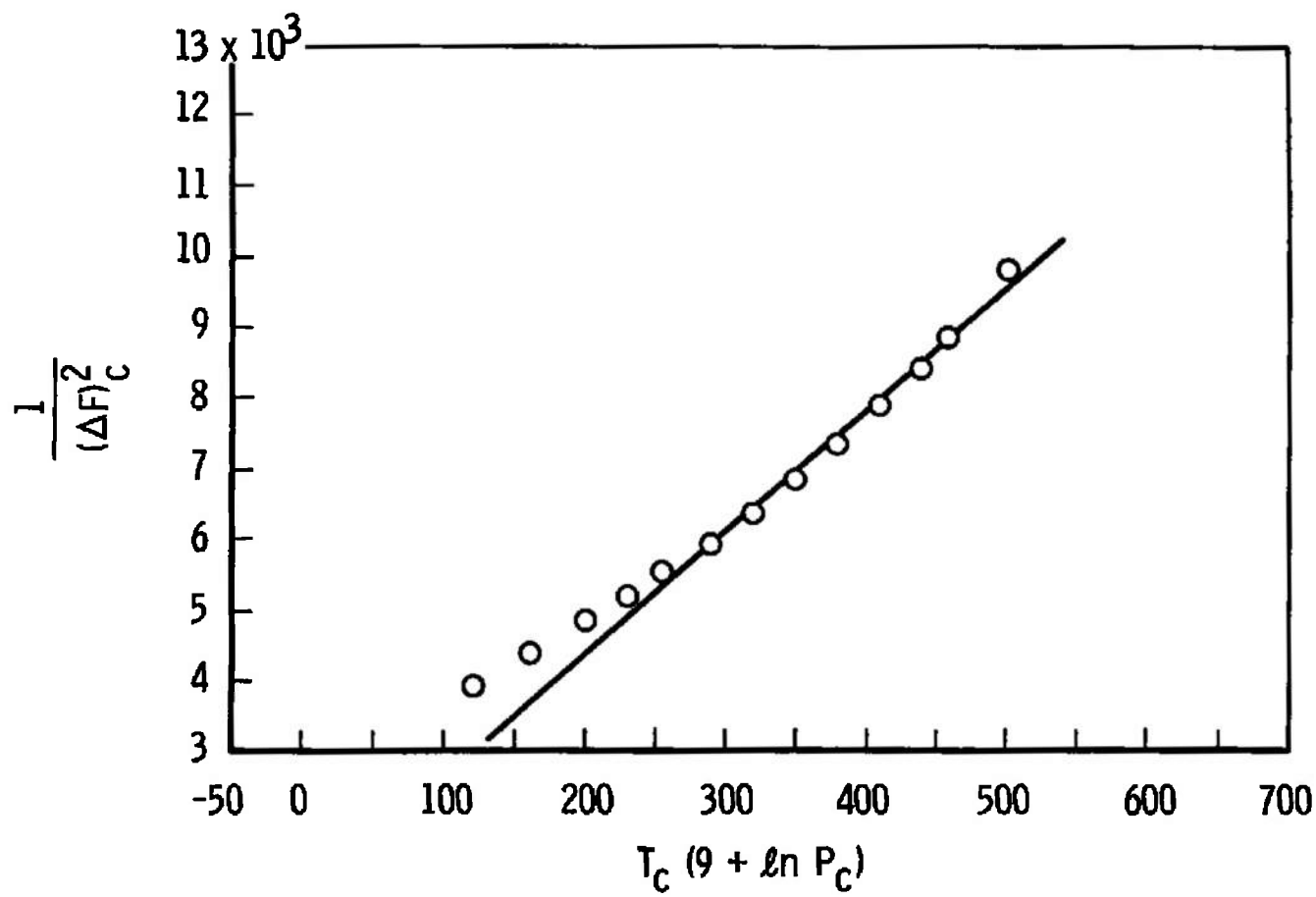


Fig. 16 Data Correlation of CO_2 to Theoretical Rate Equation

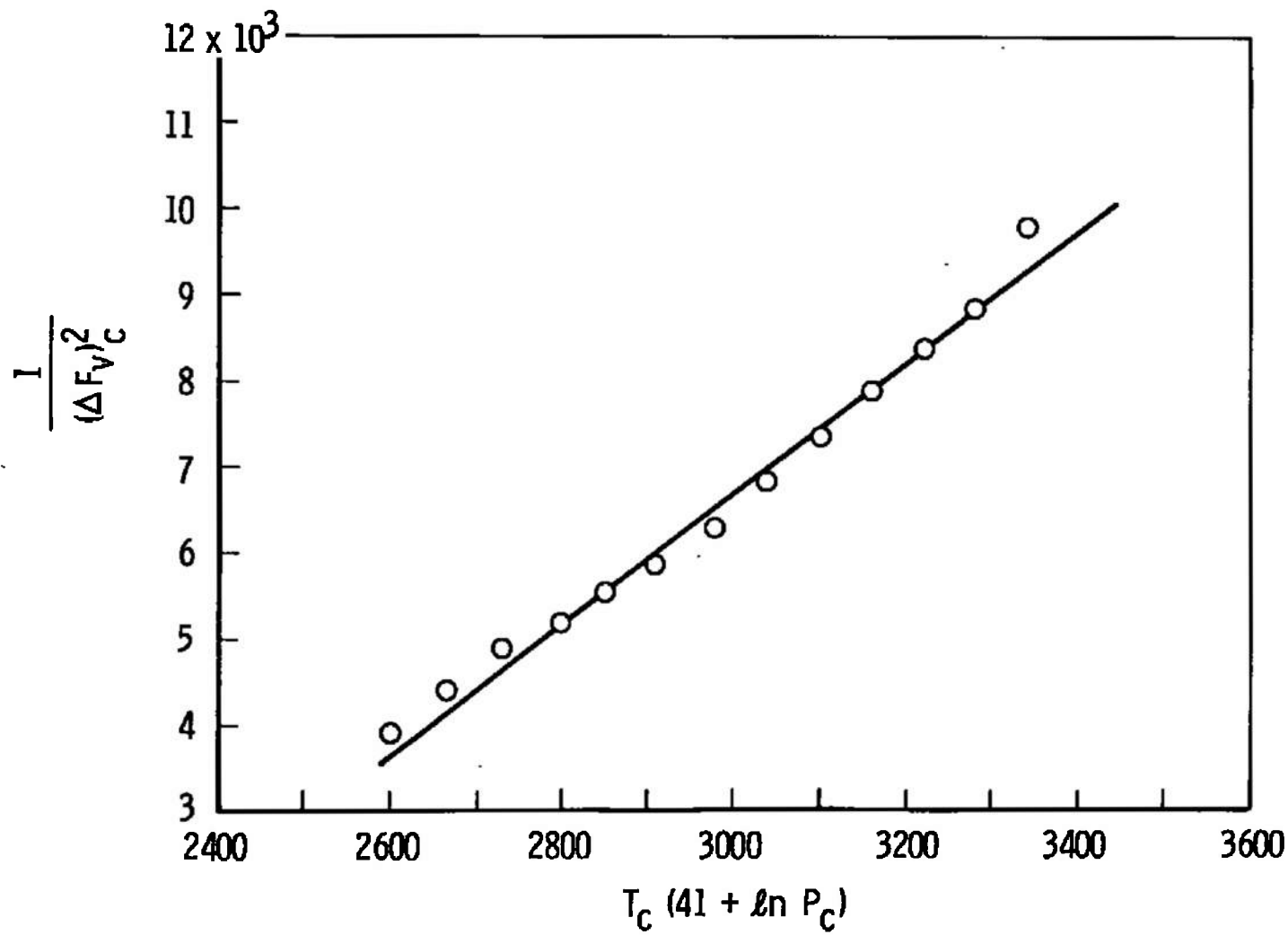


Fig. 17 Data Correlation of CO_2 to Modified Theoretical Equation

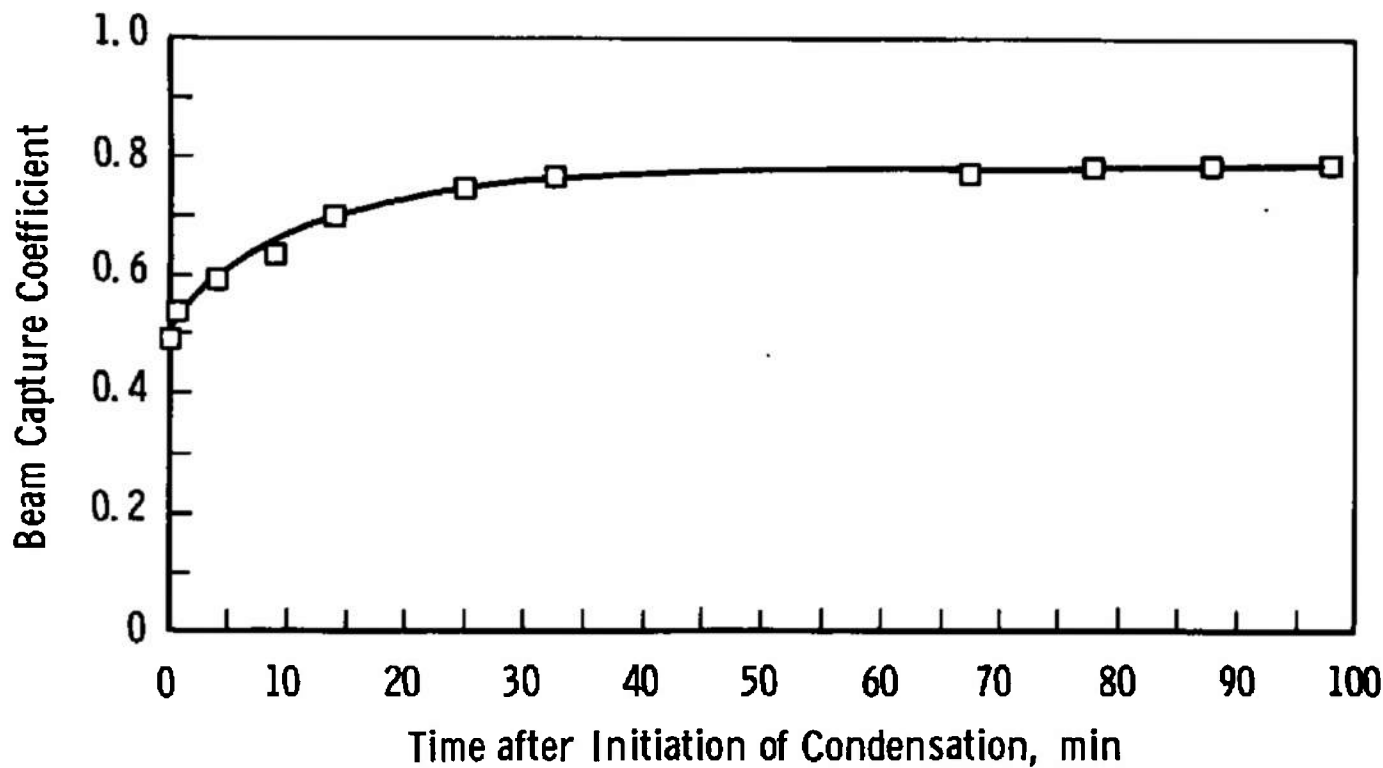


Fig. 18 Beam Capture Coefficient of CO_2 as a Function of Time
after Initiation of Condensation

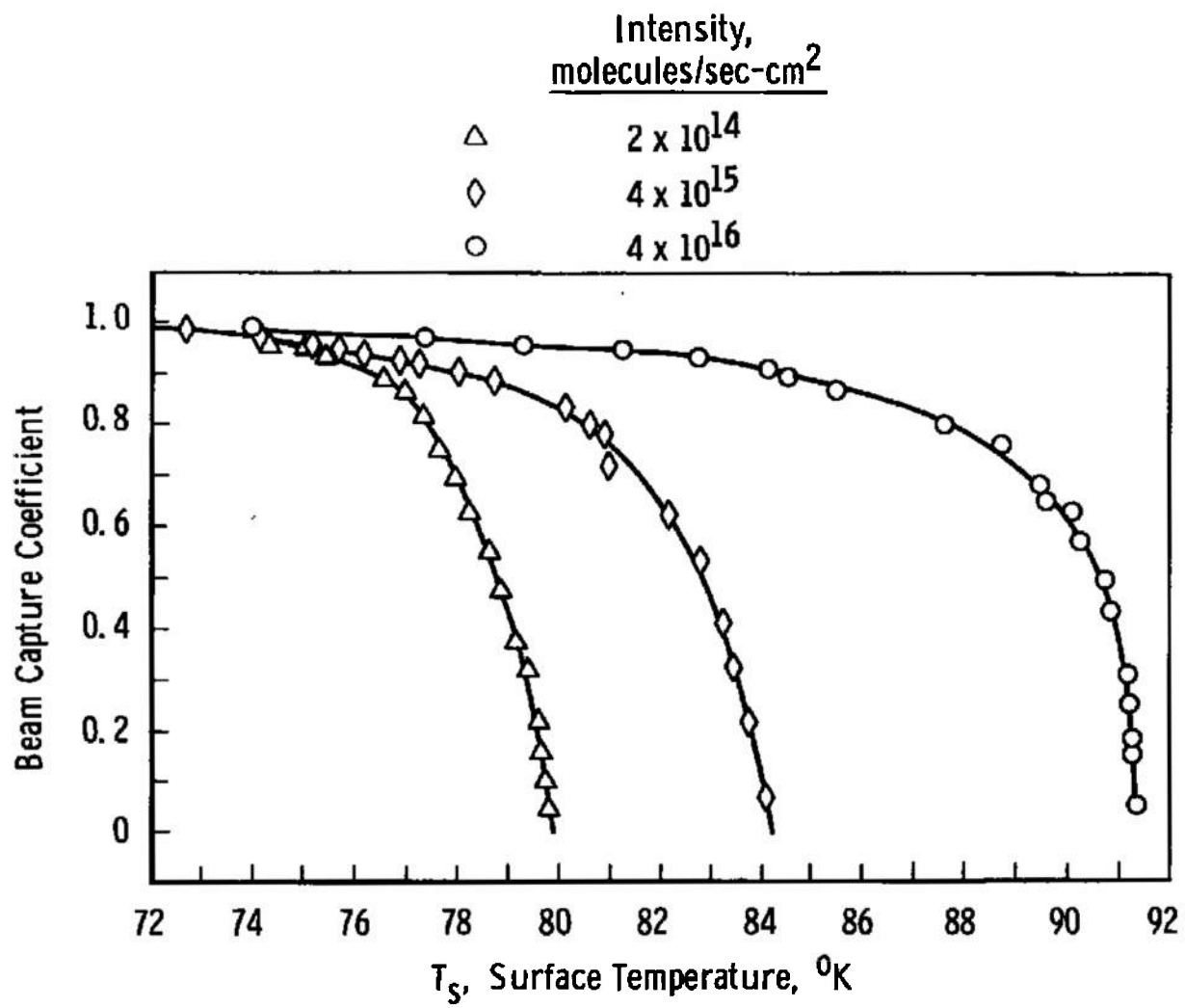


Fig. 19 Beam Capture Coefficient of CO₂ as a Function of Surface Temperature

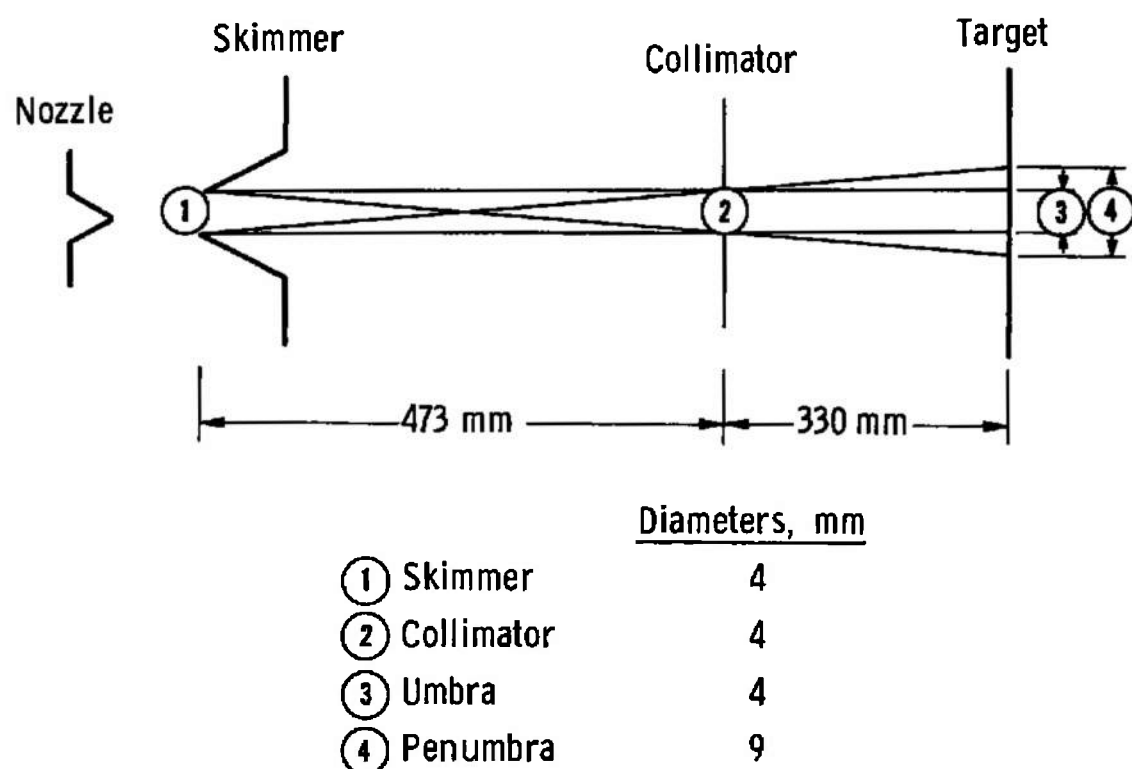


Fig. 20 Calculated Trapezoidal Beam Profile

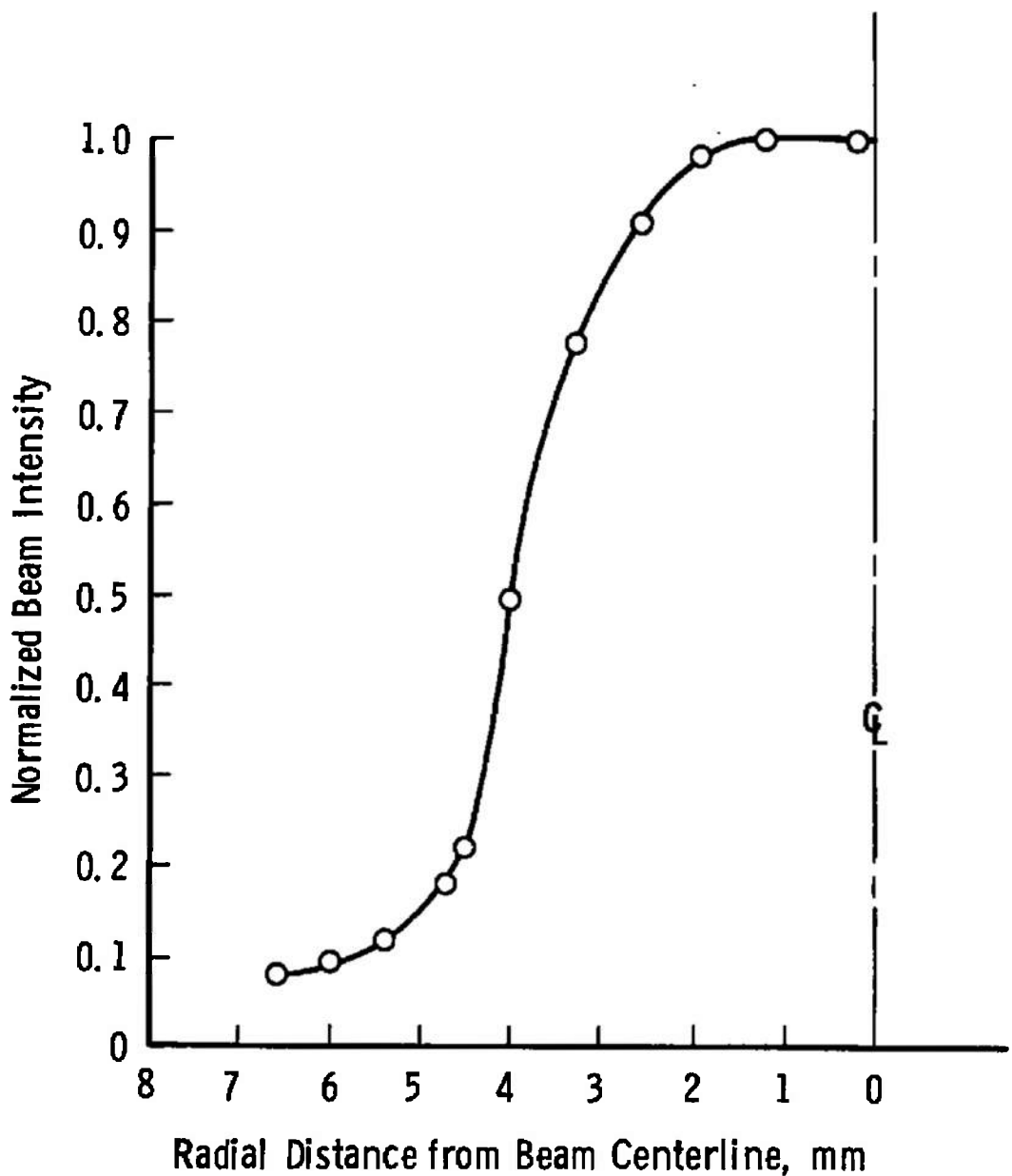


Fig. 21 Measured Incident Beam Profile

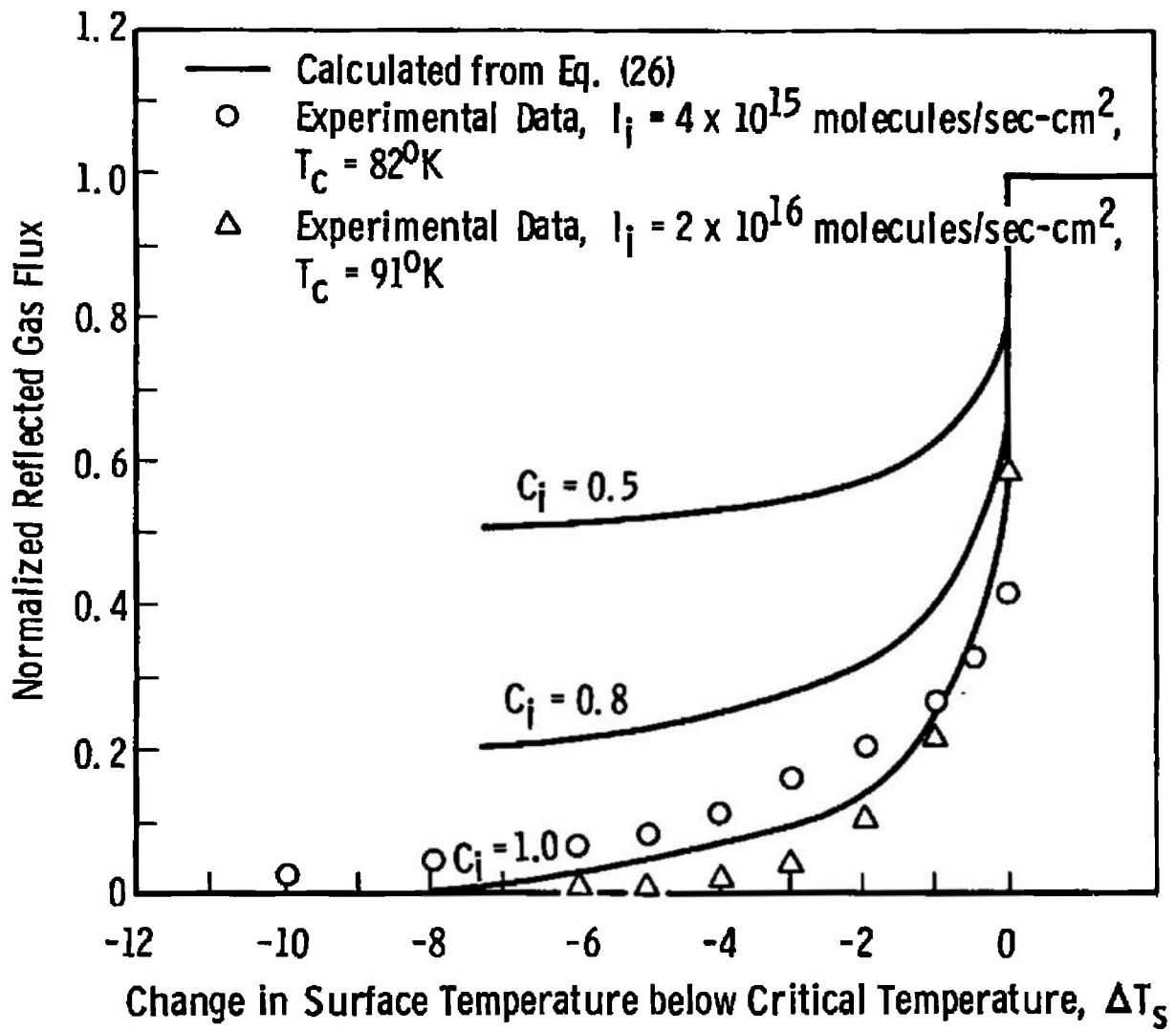


Fig. 22 Calculated Reflected Gas Flux Dependence on Surface Temperature

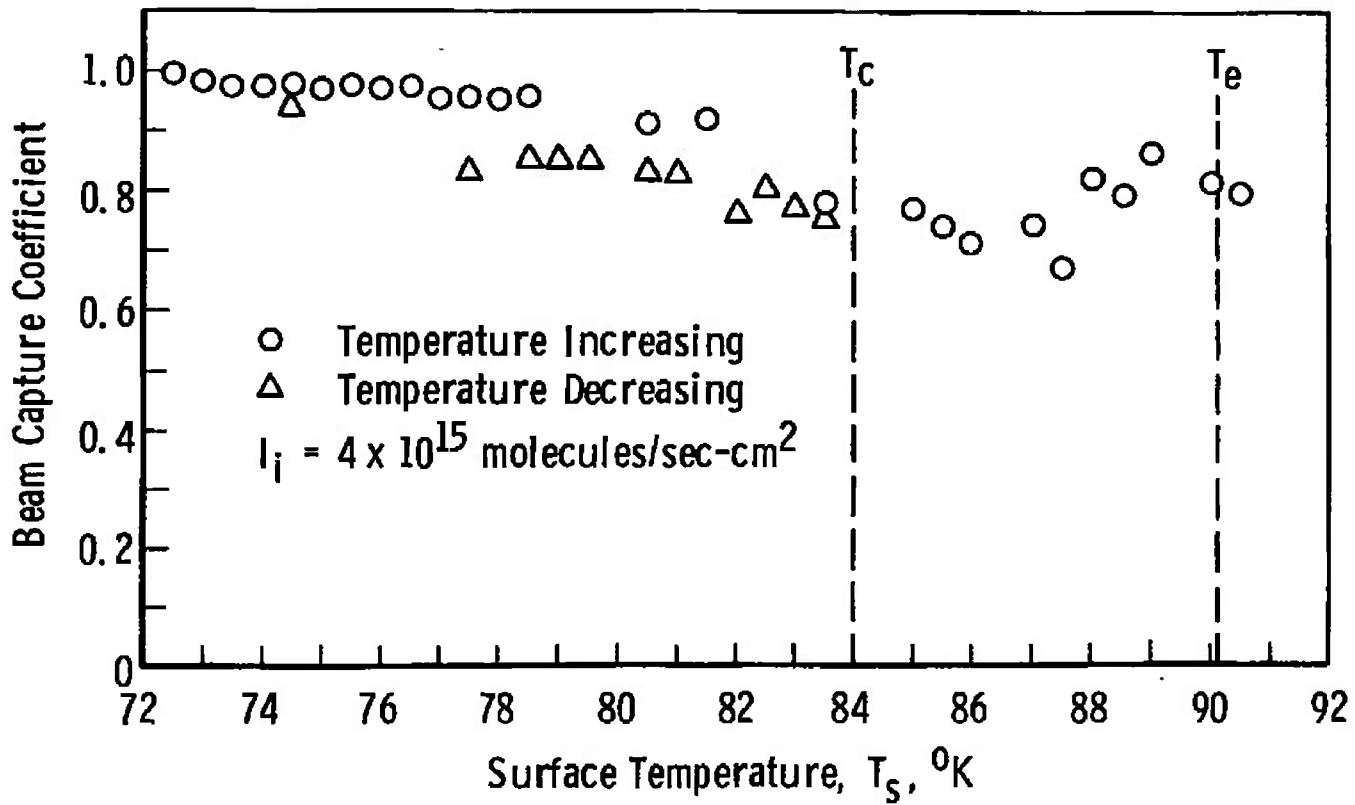


Fig. 23 Condensation Rate for High Intensity CO_2 Beam

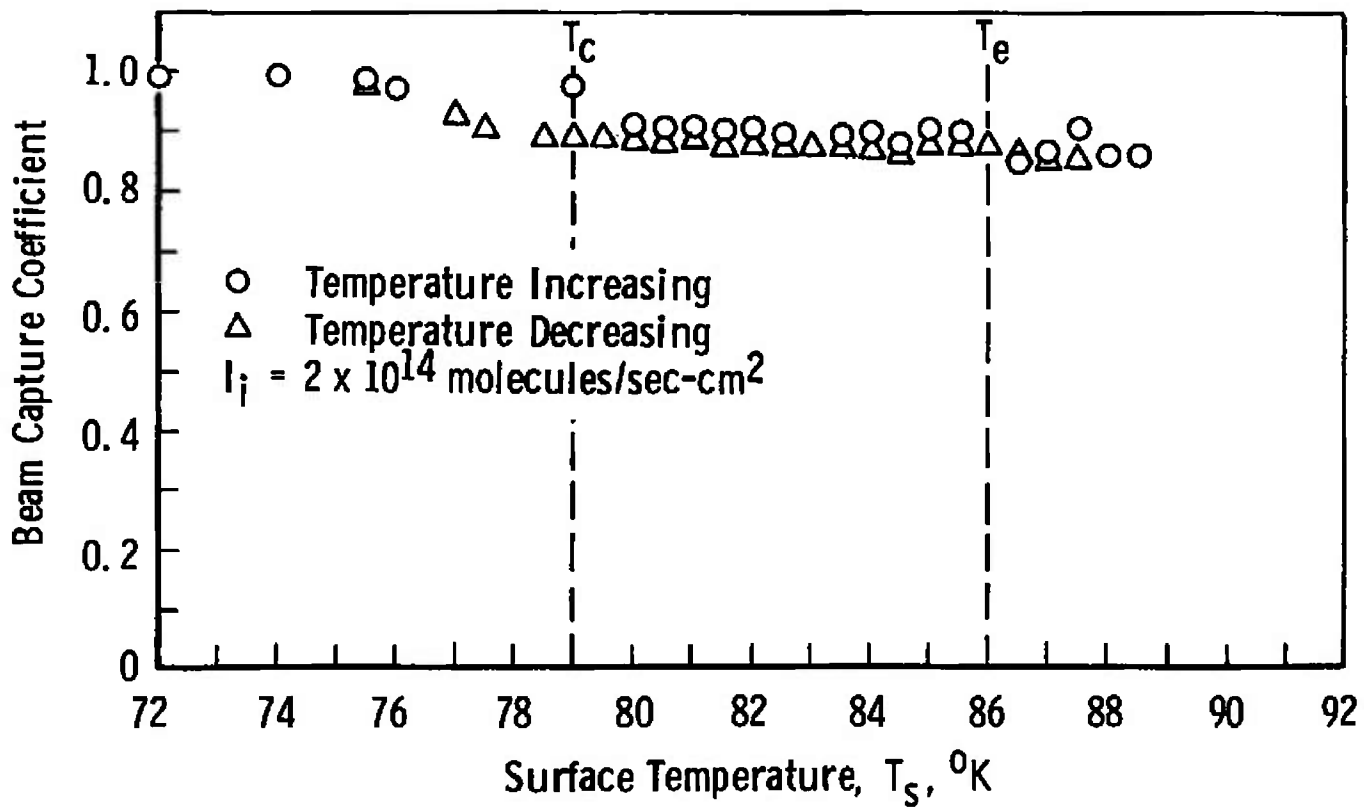


Fig. 24 Condensation Rate for Low Intensity CO_2 Beam

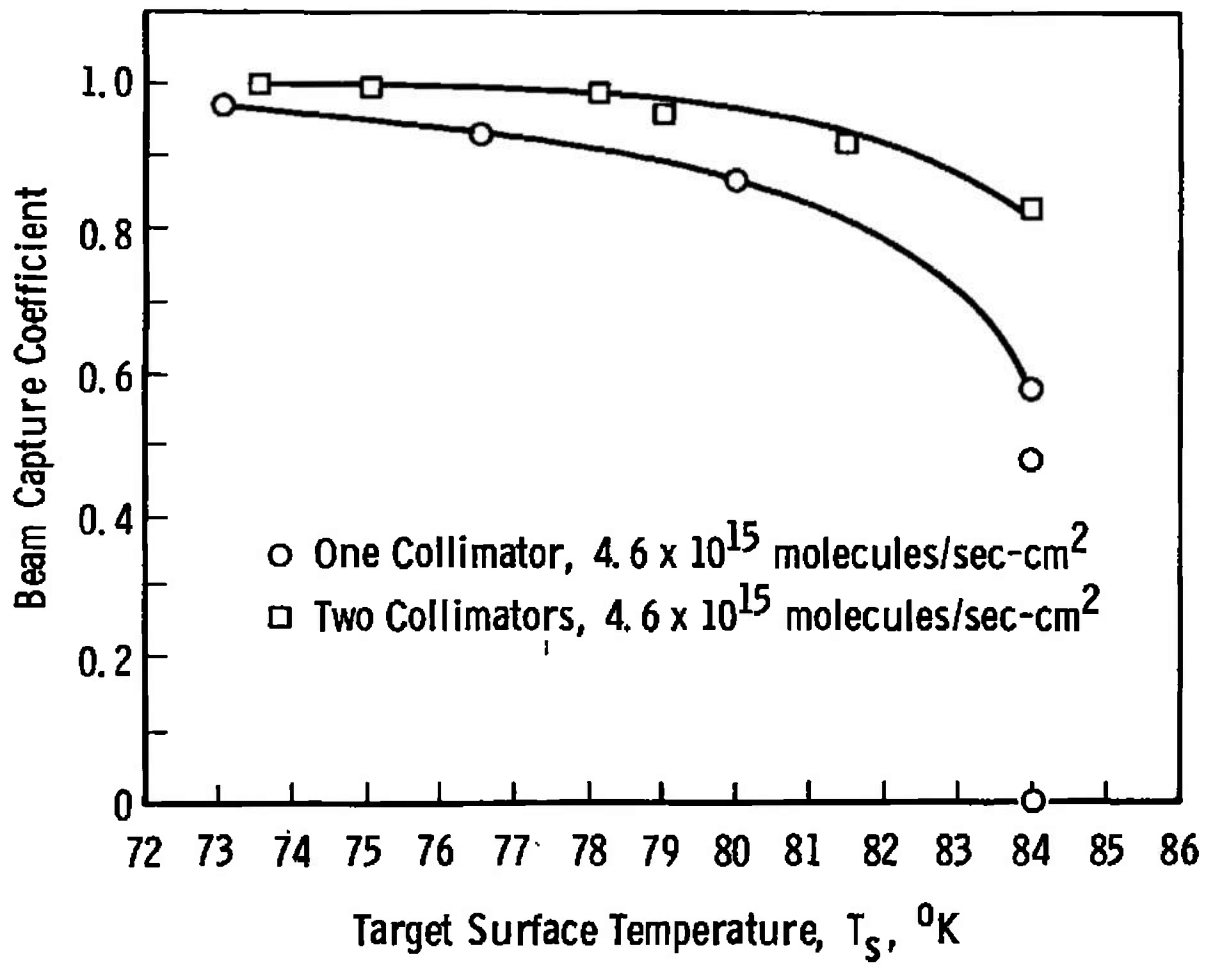


Fig. 25 Effect of Two Collimators on CO_2 Beam Capture Coefficient

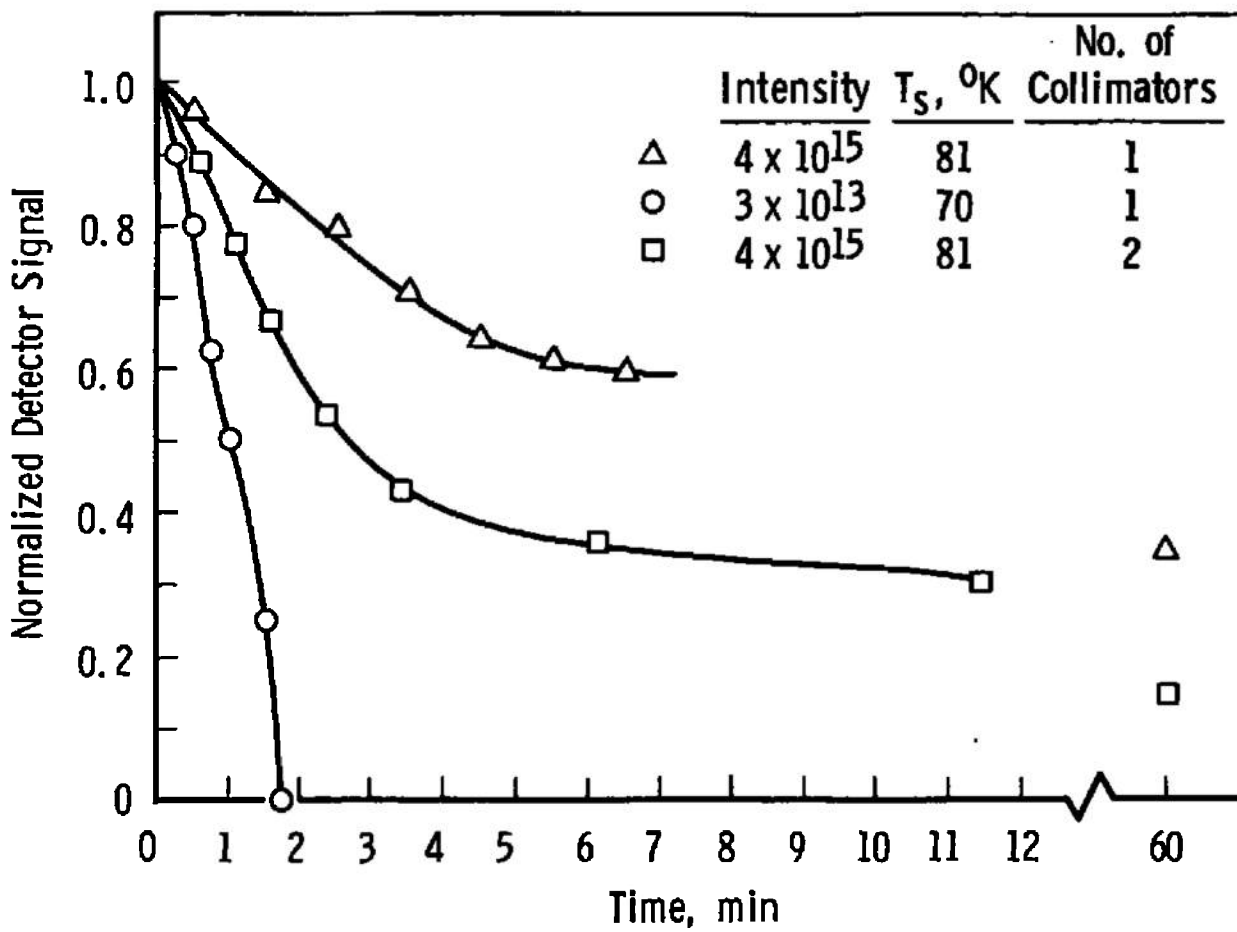


Fig. 26 Effects of Two Collimators and Beam Intensity on Time-Dependent Signals for CO_2

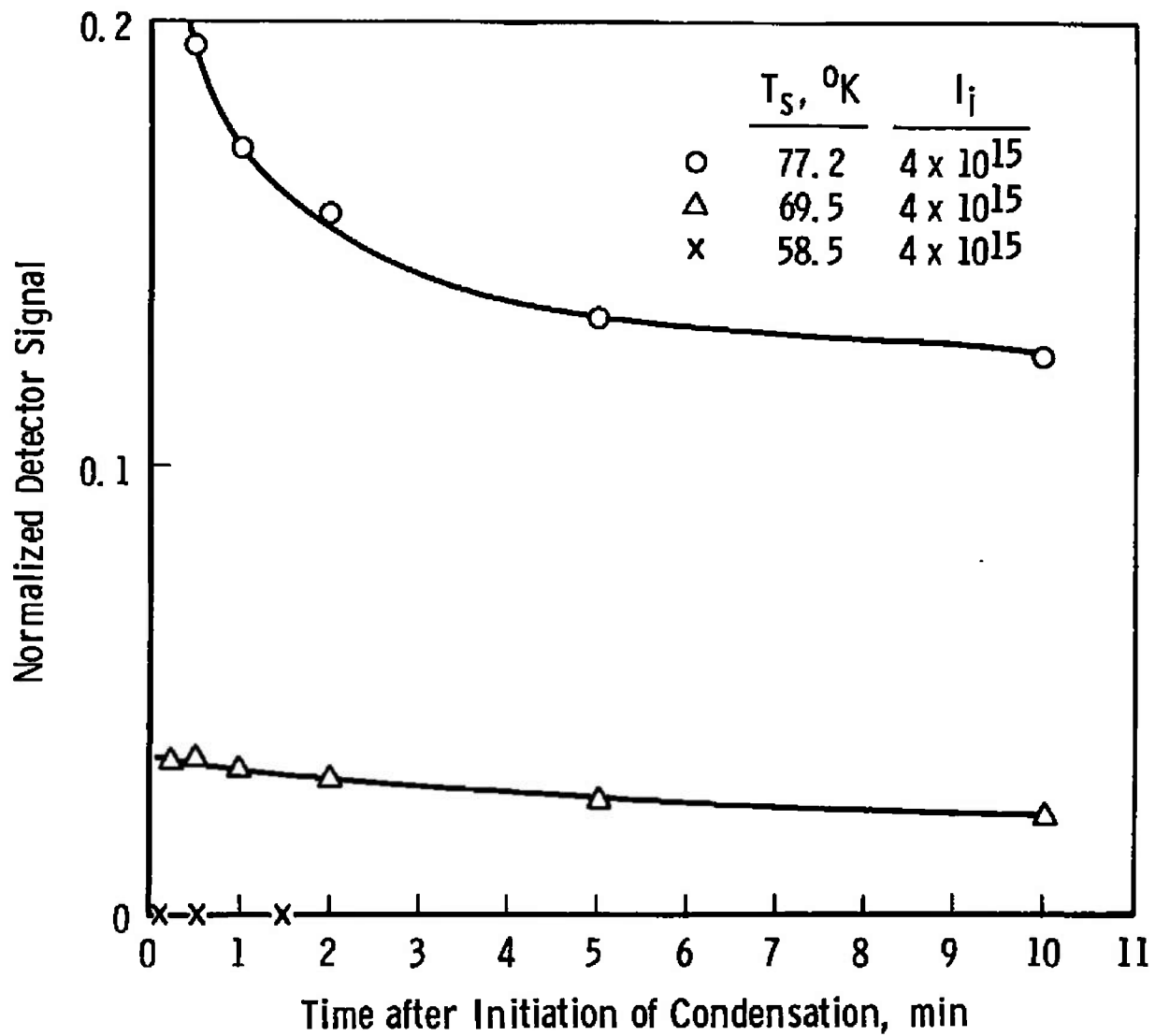
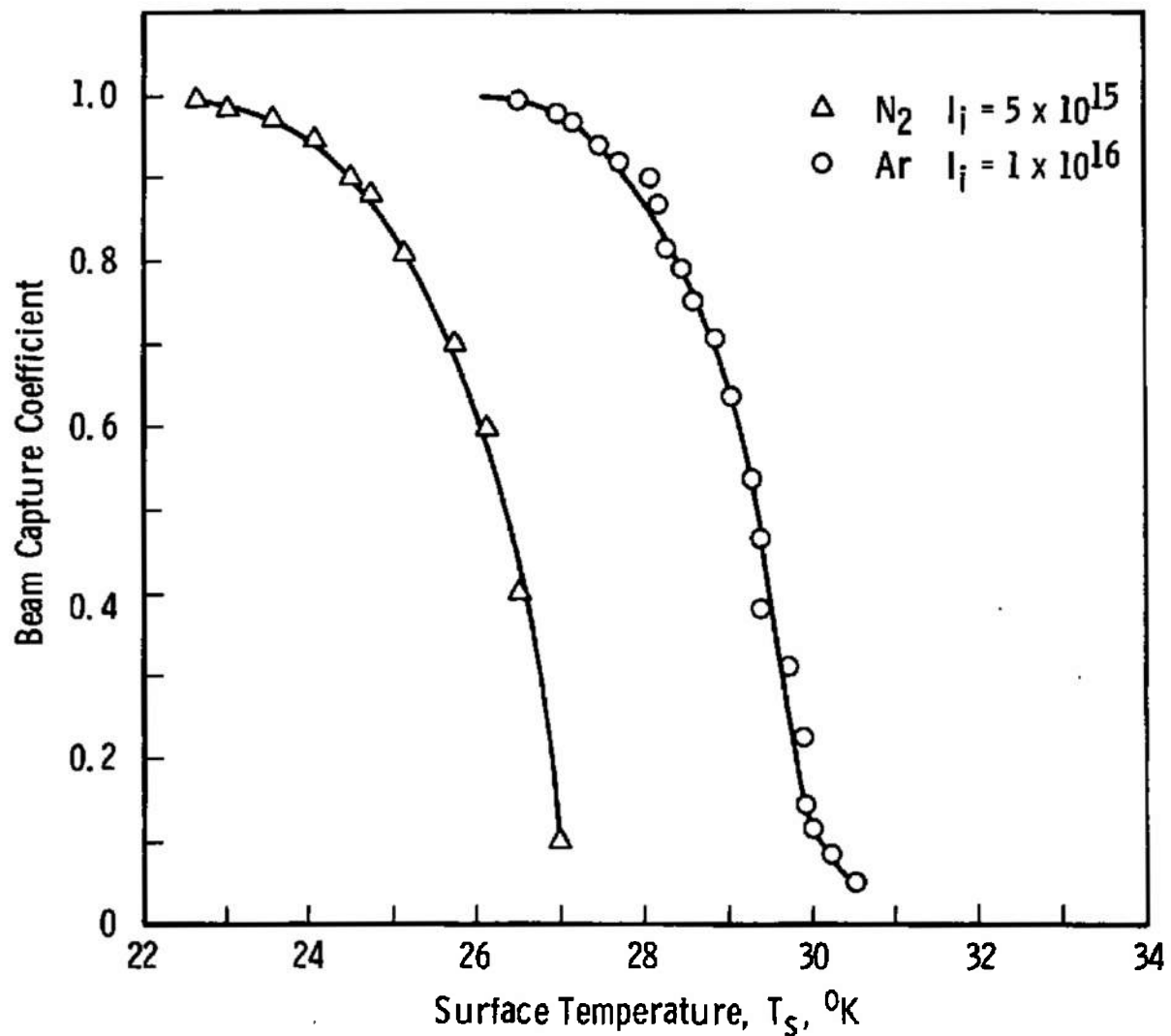


Fig. 27 Effects of Surface Temperature on Time-Dependent Signal for CO_2

Fig. 28 Beam Condensation of N_2 and Ar

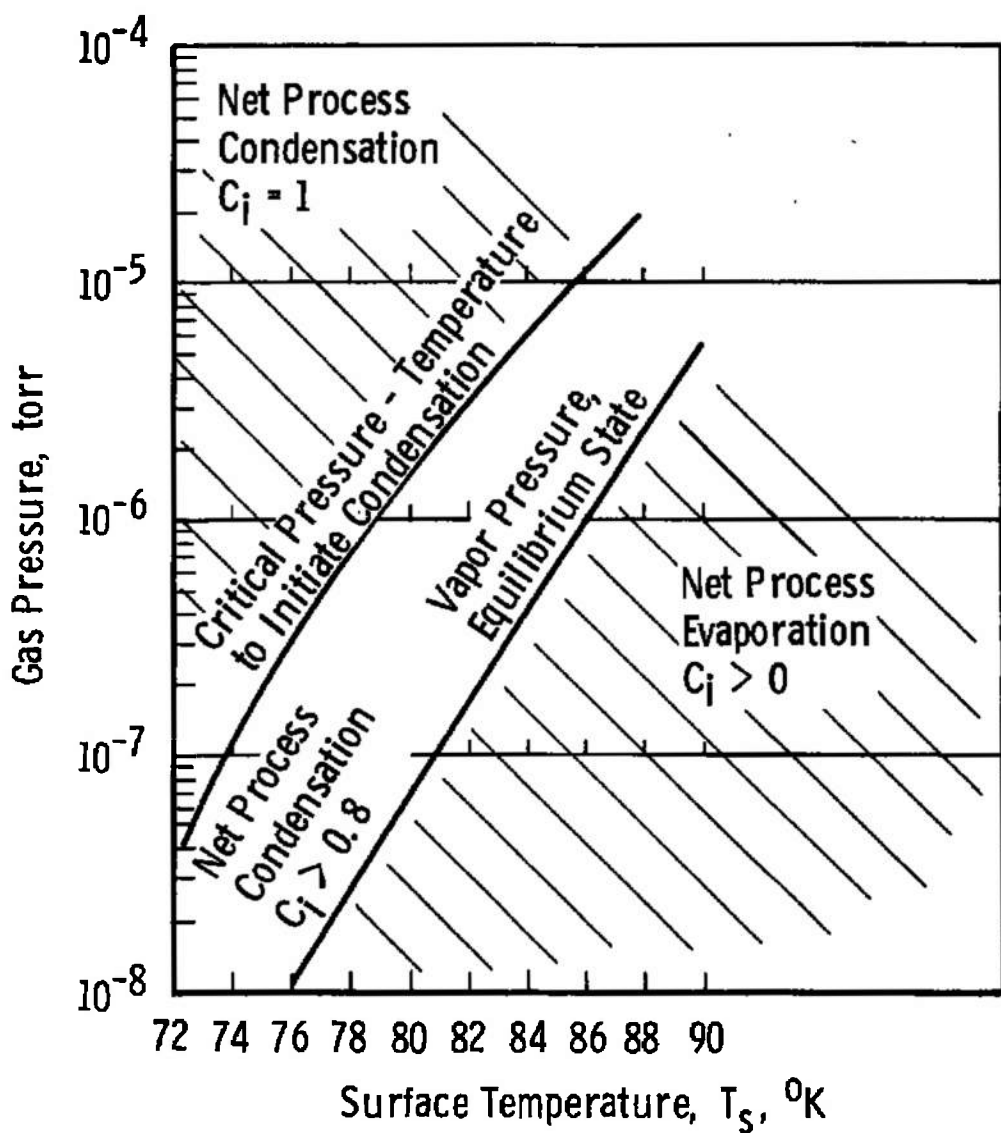


Fig. 29 General Condensation and Evaporation Regions for CO₂ between 72 and 90°K

UNCLASSIFIED

Security Classification

14 KEY WORDS	LINK A		LINK B		LINK C	
	ROLE	WT	ROLE	WT	ROLE	WT
1 condensation measurements						
2 evaporation measurements						
3 carbon dioxide —						
4 nitrogen						
5 argon						
6 molecular beams generators						
7 modulated beam detectors						
8 copper targets						
15-2						

UNCLASSIFIED